Solar-Powered Molecular Crystal μ-Motor Based on an Anthracene-thiazolidinedione Photoisomerization Reaction

Kevin Lam[(1)], Imadul Islam[(2)], Veronica Carta[1], Mohammed Almtiri[(2)], Ibrahim Bushnak[(2)], Rabih O. Al-Kaysi[(2)]*, Christopher J. Bardeen[(1)]*

[(1)]Department of Chemistry
University of California, Riverside
Riverside, CA 92521 (USA)

[(2)]College of Science and Health Professions-3124,
King Saud bin Abdulaziz University for Health Sciences, and King Abdullah International Medical Research Center (Nanomedicine), Ministry of National Guard Health Affairs, Riyadh 11426, (Kingdom of Saudi Arabia)

* corresponding authors: christopher.bardeen@ucr.edu
ORCID: 0000-0002-5755-9476
rabihalkaysi@gmail.com and kaysir@ngha.med.sa
ORCID: 0000-0001-8429-2802

Abstract

In the simplest limit, a motor takes in a continuous source of energy like electrical, thermal or light, and converts it into a well-defined mechanical response, for example unidirectional rotation at a fixed frequency. There is currently much interest in molecular machines that accomplish this transformation at the nanoscale because they could have broad applications in fields like medicine and engineering.[1,2,3] However, the directed motion of a molecular machine that operates in a condensed phase environment, like water, can be overwhelmed by Brownian forces that generate random diffusion. One way to overcome this problem is to assemble multiple active molecules into an ordered array or crystal, whose larger volume and force output can overcome Brownian forces[4,5]. But it is not clear how the motions of individual molecular engines in the crystal could be synchronized to generate directional motion on larger scales.[6] Our attempts to harness ratchet-like motion in X-shaped micro-molecular crystals made from 9-anthracene carboxylic acid were met with limited success.[7] However, the process required intermittent UV-light irradiation followed by a period of thermal relaxation (reset phase) to drive the ratchet process forward. Other attempts to harness input energy to generate directional motion from molecular crystals led to the development of novel materials know as smart crystals such as photomechanical and thermosalient crystals.[8]

The synchronization of molecular motions on macroscopic length scales is a problem of chemical kinetics. Oscillations in molecular states can lead to oscillatory dynamics in bulk chemical systems if there is a feedback mechanism that allows the reaction of one subpopulation to influence that of another. Using light as an external energy source, several workers have shown that such nonlinear chemical reactions can give rise to concentration oscillations and pattern formation. If the oscillatory chemical dynamics are coupled to the molecular mechanical degrees of freedom, then the molecular response can be harnessed to drive mechanical motion up

to macroscopic length scales. Light-driven oscillatory motion has been observed for photomechanical materials composed of azobenzene-containing polymers or crystals, where it has been ascribed to oscillations in the Z/E populations that give rise to a time-varying stress in the material. These motions typically require specific illumination conditions, with the angle of light incidence and polarization fixed by the need for self-shadowing to modulate light absorption. Furthermore, the oscillatory motion often relies on photothermal heating to accelerate the Z→E backreaction, so the motion is sensitive to the heat conduction properties of the surrounding medium. In many cases, changing the thermal transport properties of the environment (e.g. by placing the sample in water) can be enough to suppress the oscillatory motion. In order to develop functional assemblies of light-powered molecular machines, it is desirable to have a system whose forward and reverse isomerizations are exclusively light-driven and whose motion is robust with respect to conditions like light polarization and direction.

We recently demonstrated that single crystals composed of cis-**DVAM** exhibited oscillatory wiggling and twisting when exposed to a combination of visible (532 nm) and ultraviolet (405 nm) continuous light sources (lamps)[9,10]. The forward and reverse E-Z reactions were both purely light-driven, but the widely separated absorption maxima of the E and Z isomers necessitated the use of separate wavelength sources. This system required two different light sources and polarization control, as well as growth of a starting crystal composed of the less stable Z-isomer (or cis-isomer),

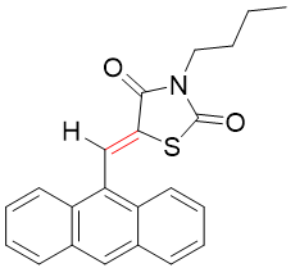

"Z" **C4-ATD**
This work

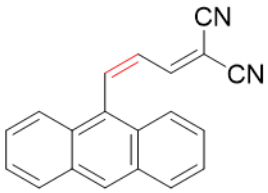

cis-DVAM

The existence of widely separated reactant and product absorption spectra is desirable for applications like data storage but significantly complicates the use of light as a fuel.[11] In order to use a single wavelength of light to drive reactant and product populations back and forth, a photoisomerization reaction that does not give rise to a substantial absorption shift would be more useful. But this isomerization should still give rise to a physical distortion of the molecule that can drive photomechanical motion. To meet these requirements, we synthesized the molecule (Z)-5-(anthracen-9-ylmethylene)-3-butylthiazolidine-2,4-dione (**C4-ATD)** following the procedure shown in Scheme 1. Details of the synthesis and characterization are given in the Supporting Information. Briefly, a Knoevenagel condensation[12] reaction involving commercially available 9-anthraldehyde and thiazolidine-2,4-dione produced (Z)-5-(anthracen-9-ylmethylene)thiazolidine-2,4-dione in moderate yield.[13] The presence of a relatively acidic N-H hydrogen in (Z)-5-(anthracen-9-ylmethylene)thiazolidine-2,4-dione provided an opportunity to synthesize alkyl chain derivatives for improved solubility. To verify this, the resulting product was reacted with an excess of 1-bromobutane in the presence of anhydrous N, N-Dimethylformamide as the solvent and potassium carbonate (K_2CO_3) as the deprotonating base. This series of reactions culminated in the formation of the desired product, **C4-ATD**, which we further purified through recrystallization in a mixture of acetonitrile and water.

The Z→E photoisomerization of **C4-ATD** is similar to that of the hemi-indigos previously reported by Wolf and coworkers.[14] The photochemistry of **C4-ATD** in both the solid state and solution primarily involves the Z→E photoisomerization about the olefin bond that connects the anthracene and the thiazolidinedione head group. Although the extent of Z→E photoisomerization did not surpass 50% in solution due to the overlapping absorption spectra of both isomers, our analyses, encompassing ^{1}H NMR (Figure S7) and HPLC (Figure S5), confirm the nature of this photochemical transformation. The E isomer of **C4-ATD** is kinetically stable in solution and in the solid-state, with no apparent thermal isomerization to the Z form even after a week at room temperature. We suspect the kinetic stability of the E isomer results from the fact that the thiazolidinedione headgroup can mitigate steric interactions with adjacent anthracene hydrogens by adopting a twisted conformation.

The main advantage of **C4-ATD** for molecular crystal motor development is that its two isomers have almost identical absorption spectra in solution, both in terms of peak wavelength and in terms of absorption coefficient, as shown in Figure 1. The main difference between the two isomers is the orientation of the transition dipole moment (TDM) with respect to the anthracene 9-10 carbon axis, as illustrated in the Figure 1 inset. The TDM is calculated to rotate from 28º in the Z-isomer to -9º in the E-isomer. This rotation of the TDM is similar in magnitude to that of cis-**DVAM**, and in previous work we showed that a TDM rotation, when coupled to a crystal rotation or twisting, can give rise to oscillatory motion.[9]

Preparation of a photochromic molecule with favorable spectroscopic properties is not sufficient to create a molecular crystal motor, however. In the crystal, this molecule must a) adopt a packing geometry that enables the photoisomerization; and b) grow into a crystal shape that allows macroscopic motion to be observed.[15–18] Fulfilling condition a) required adjusting

the crystallization conditions to grow a polymorph that supports the photoisomerization reaction. The reactive polymorph **A** (Figure 2a, b) can only be grown in aqueous surfactant conditions, while the unreactive form **B** (Figure 2c, d) is obtained under standard crystal growth methods like solution evaporation and sublimation. Examination of the two structures shows that in polymorph **B** the anthracene rings interfere with rotation of the thiazolidinedione rings that is necessary for photoisomerization. The reactive polymorph **A**, on the other hand, has the thiazolidinedione rings lined up to form a corridor of flexible moieties that can easily rotate upon light exposure. The stacked packing motif of polymorph **A** leads to a preferred growth habit that enables the growth of quasi-one-dimensional crystals that adopt the shape of long wires or ribbons. The SEM images in Figures 2e and 2f show both types of morphologies, which can be obtained selectively by modifying the growth conditions. This morphology leads to structures with a low bending moment of inertia and facilitates the deformations that modify its light absorption properties. The absorption spectra collected from a thin film of the **A**-form microcrystals showed considerable broadening but only about a 10 nm redshift of the main absorption peak, suggesting that the electronic states of the molecule in the crystal are is similar to those of the isolated molecule.

When exposed to 405 nm light, **C4-ATD** crystal wires and ribbons undergo an undulating motion that reflects a variable twist period along the length of the crystals. The motions of both morphologies are illustrated in Figure 3. Note that these motions can also give rise to a center-of-mass translation of the entire crystal, as can be seen from the motion of the ribbon in Figure 3f-3h relative to a stationary object in the lower left corner of the frame. The oscillatory motion continued indefinitely for all illumination conditions. We suspect that the surrounding water removes excess heat generated by the absorption, helping prevent fatigue or thermally-induced

transition to crystal form **B**. The aqueous environment also served to enable the suspended crystals to freely move and sustain the light-induced motion. Motion was not observed for dry wires lying on a glass surface, probably due to surface adhesion that was stronger than the photomechanical forces. However, oscillatory motion from microwires anchored to a solid support and freely suspended in space was observed but inconsistently. This observation rules out the influence of aqueous media on the oscillatory behavior of these microwires.

The ability of single light source to drive continuous motion represents the main advance in this paper. It arises from the similar absorption spectra of the two isomers, and any light source should be able to drive the motion. The balancing of forward and backward rates is accomplished by the molecule, as opposed to structuring the light source. We tested this ability by using a broadband solar simulator light source to drive crystal motion. The resulting oscillatory motion is shown in Figure 3. Oscillatory motion can be induced even under ambient solar light intensities, with a frequency of $0.2\ s^{-1}$ observed for a solar intensity of $0.1\ W/cm^2$. It is surprising that this very simple chemical system can exhibit lifelike motion under ambient sunlight conditions.

The frequency of oscillation depended on the incident light intensity, as shown in Figure 4a. Under 405 nm, the frequency increased linearly after a threshold value of ~0.5 mW/cm^2 is reached. At higher intensities, the slope decreased, showing the same signs of saturation observed previously for the cis-**DVAM** oscillations. Interestingly, under broadband solar light, no saturation behavior was observed. Given the fact that most of the solar simulator spectrum falls outside the **C4-ATD** absorption, we think that the effective intensity available for photoisomerization is much less than the total measured intensity, so the oscillation frequency is still in the linear regime, well below the 3 s^{-1} level where it saturates under monochromatic 405

nm irradiation. This saturation behavior has been observed previously and results from the basic process that leads to saturation in other photophysical processes like absorption. If the motion were due to photothermal heating, then the frequency would increase linearly with light intensity until the crystal melted.

The **C4-ATD** crystal oscillations were much less sensitive to light polarization than the previously studied cis-**DVAM** crystals. For **C4-ATD** the dependence of the oscillation frequency on the 405 nm polarization direction relative to the crystal long axis was close to isotropic (Figure 4c), as opposed to the $\cos^2$ dependence characteristic of a single dipole-allowed transition. This lack of directionality results from the fact that the 405 nm light simultaneously excites two different isomers with different TDM orientations. The presence of two different TDM directions effectively scrambles the polarization dependence in much the same way that different overlapping transitions scramble the fluorescence anisotropy from a single crystal.

HPLC analysis of Z-isomer crystals exposed to 405 nm light for an extended period (>5 min) showed a conversion from Z to E of ~4%. This is much less than the conversion observed for **C4-ATD** in solution (Figure S5), which is close to 50%. The solution data reflects a true stationary state, an equilibrium is reached when the forward and backward reaction rates (determined by the absorption cross sections and quantum yields) equalize. The crystal reaction, on the other hand, never reaches a true stationary state because it is always oscillates back and forth between Z and E populations. Direct measurement of the dynamic Z and E population changes within a single oscillating crystal would confirm this but is reserved for future work.

The exact mechanism of the oscillatory motion requires further investigation. To model the dual wavelength **DVAM** results, we hypothesized that the oscillatory motion of **C4-ATD** crystals involved a feedback loop between the photochemistry, which twisted the crystal and

rotated the TDMs in the lab frame, modulating the ability of the molecules to absorb incoming radiation. This changed the balance between forward and backward reaction rates. We can use the same model to describe the **C4-ATD** data, with parameters set by the TDM orientations and absorption cross sections. The results of some sample calculations are presented in the Supporting Information, along with the parameters used, to show that this model qualitatively reproduces the experimentally observed behavior.

Conclusion:

In this paper, we reported the synthesis and characterization of a new type of photoisomerizable molecule, **C4-ATD**, whose Z→E isomerization induces large geometry changes but only slight changes in its absorption profile. By assembling this molecule into the correct crystal polymorph and shape, it exhibits robust and autonomous photomechanical oscillations under a variety of conditions, including normal solar irradiation. Preliminary experiments on other alkyl chain derivatives that contain the **ATD** motif suggest that oscillatory motion is a general characteristic of this family of molecular crystals. The combination of photochrome design and crystal engineering enables the concept of molecular machines fueled by light to be extended to molecular crystals, whose directional work can easily overcome Brownian noise in room temperature liquids.

Acknowledgements

R.O.K. acknowledges the support of KSAU-HS/ KAIMRC through grant NRC21R25003. C. J. B. acknowledges support by the National Science Foundation through grant DMR-1810514.

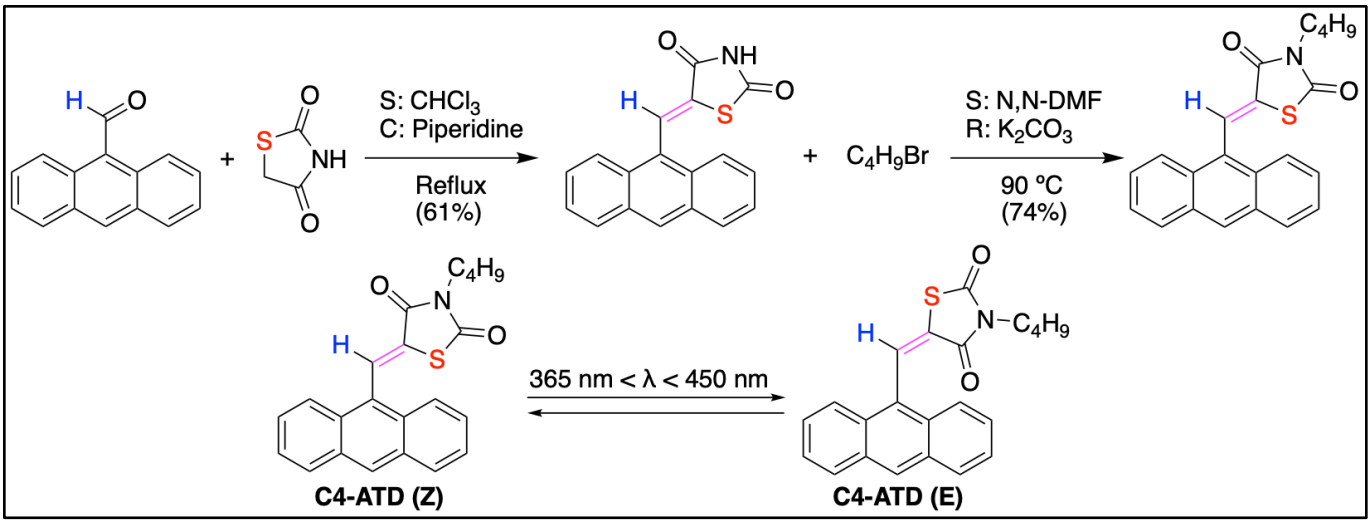

Scheme 1. Synthesis of (Z)-5-(anthracen-9-ylmethylene)-3-butylthiazolidine-2,4-dione **C4-ATD** and its photoisomerization reaction scheme.

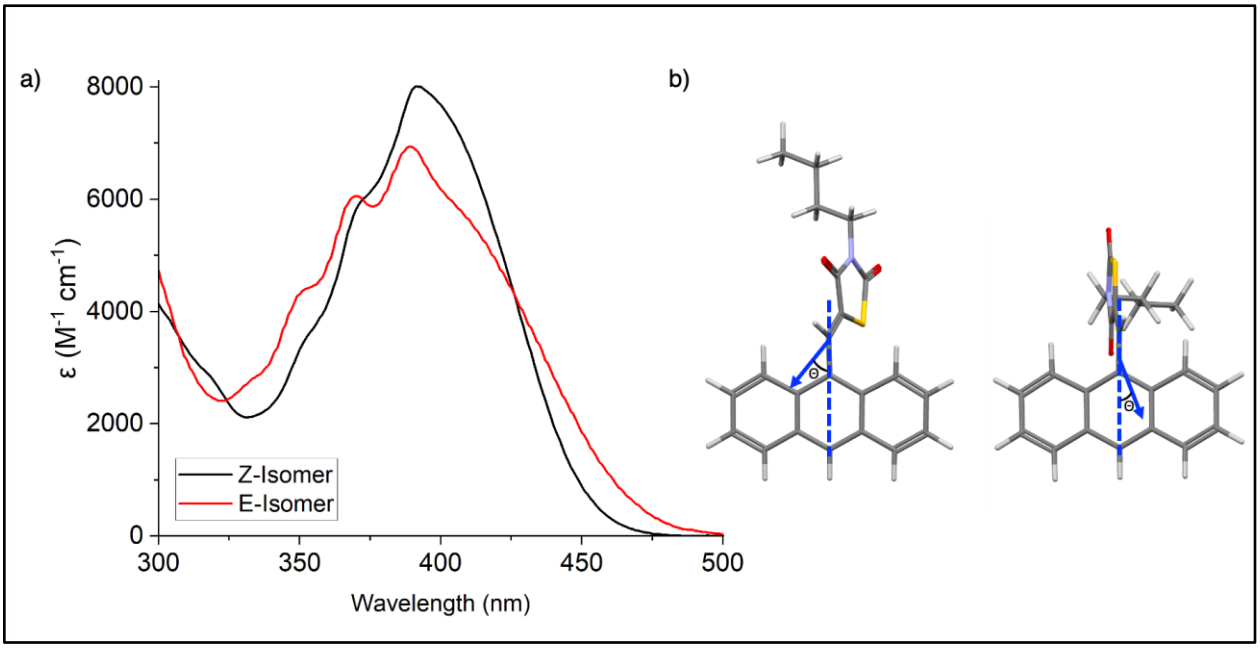

Figure 1. a) UV-Visible absorption spectra of pure Z-**C4-ATD** and its pure photoisomer E-**C4-ATD** in Acetonitrile b) Schematic illustrating the approximate transition dipole

moments of both isomers (Z and E isomers respectively) calculated in the gas phase at the CAM-B3LYP/6-311++G(d,p) level of theory.

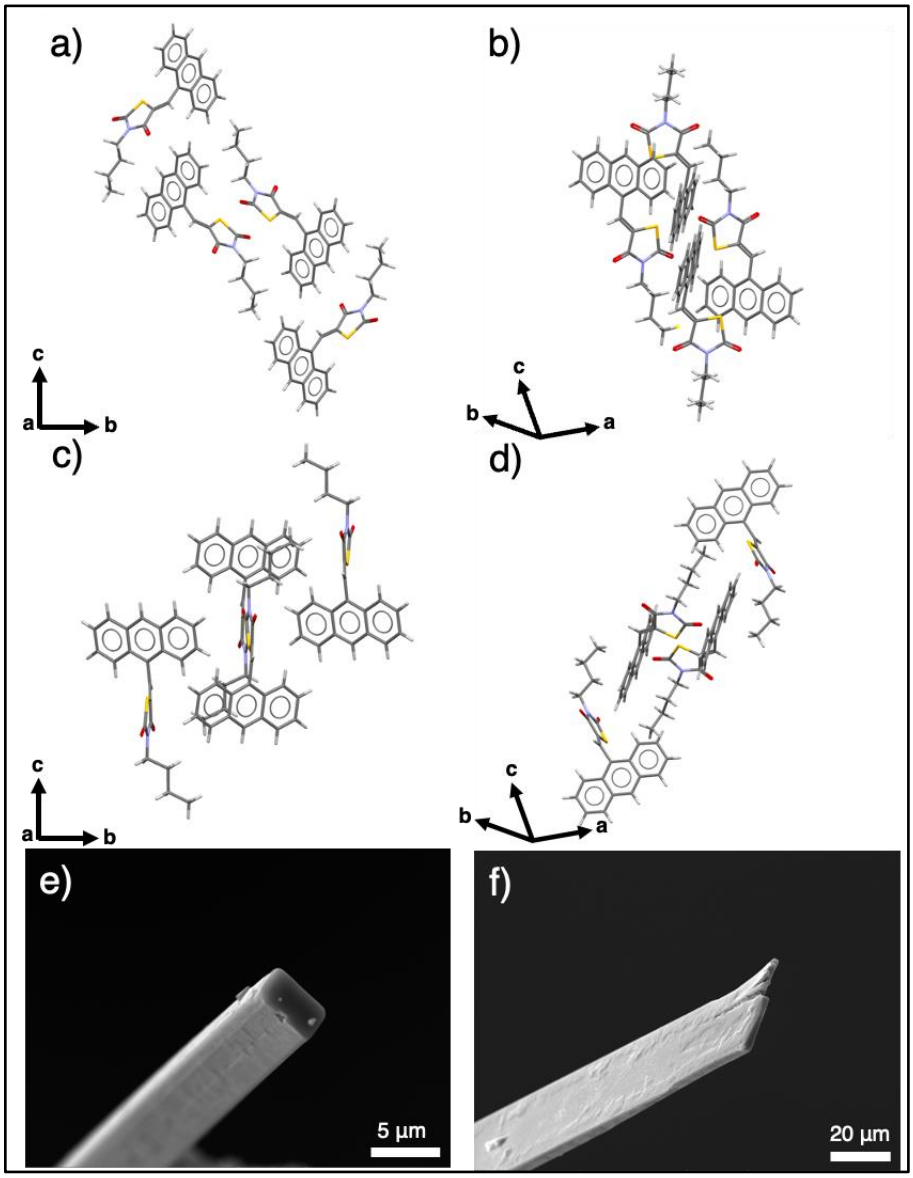

Figure 2. Crystal structures of the active (a,b) and inactive (c,d) polymorph of **C4-ATD**. SEM cross sections of the active polymorph are shown with aspect ratio e) 1:2.1 and f) 1:7.3.

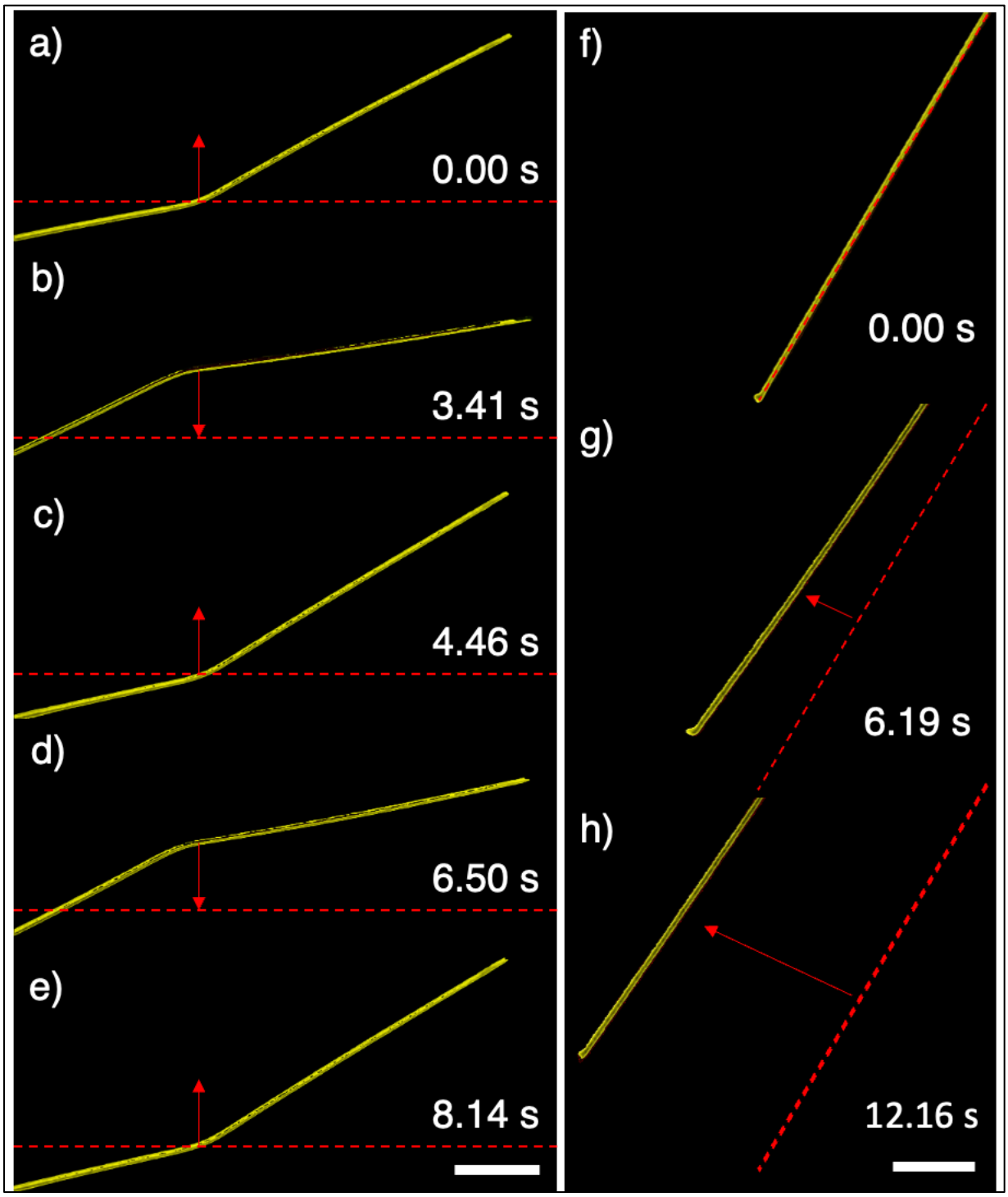

Figure 3. Sequential microscopy images showing oscillatory ratchet-like motion (a-e) and translational motion (f-h) of a **C4-ATD** microwire under UV light (405 nm, 99.6 mw/cm^2). Scale bar: 100 μm.

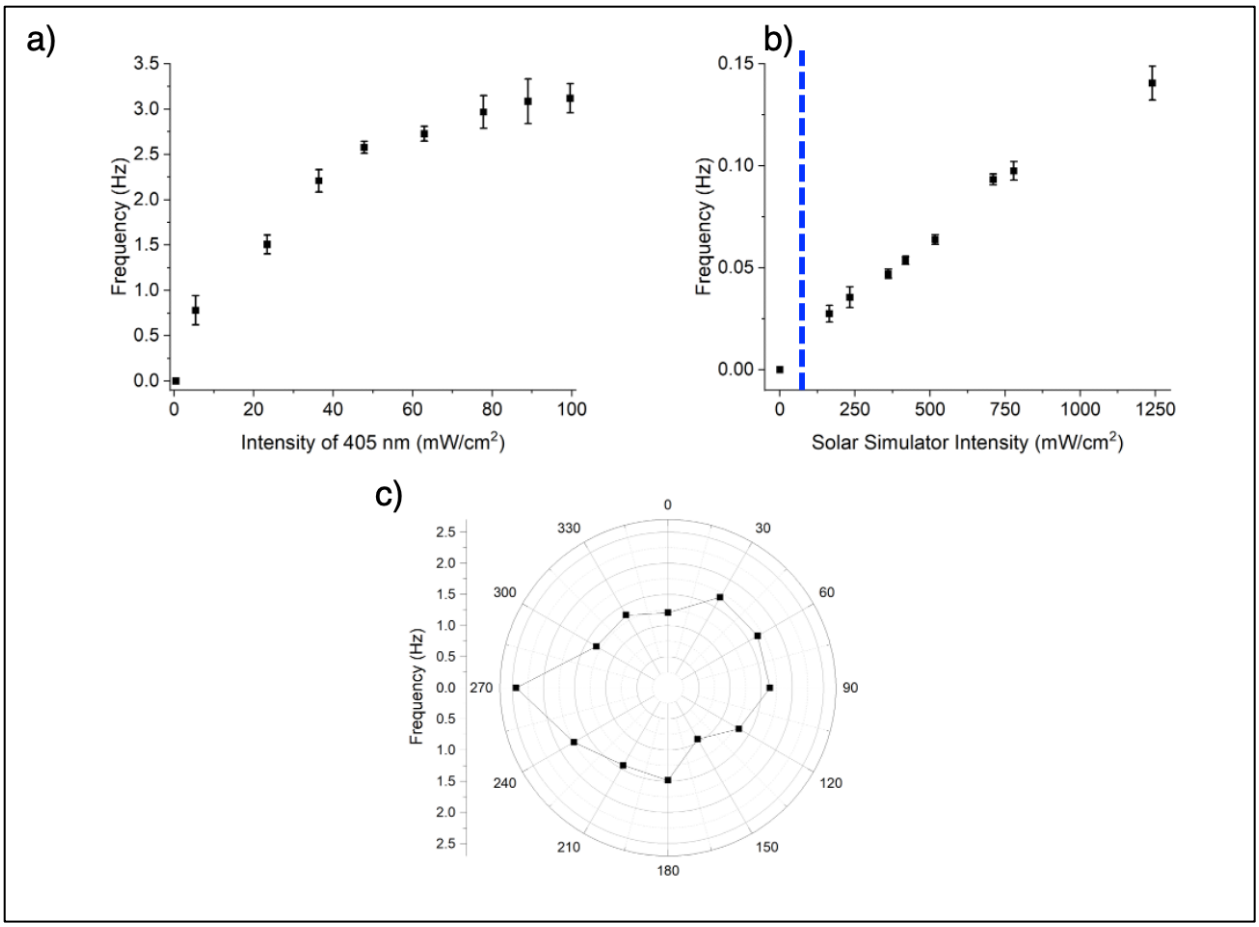

Figure 4. Frequency dependence of a **C4-ATD** microwire under a) unpolarized 405 nm light (left) and b) simulated sunlight (right); c) Effect of polarized 405 nm light on the frequency of oscillation for two different microwires. The blue dotted line represents the spectral intensity on an average sunny day.

Note: No oscillation was observed for these following intensities:

405 nm – 0.45 mW/cm^2

Solar Simulator – 5.4 mW/cm^2 & 28 mW/cm^2

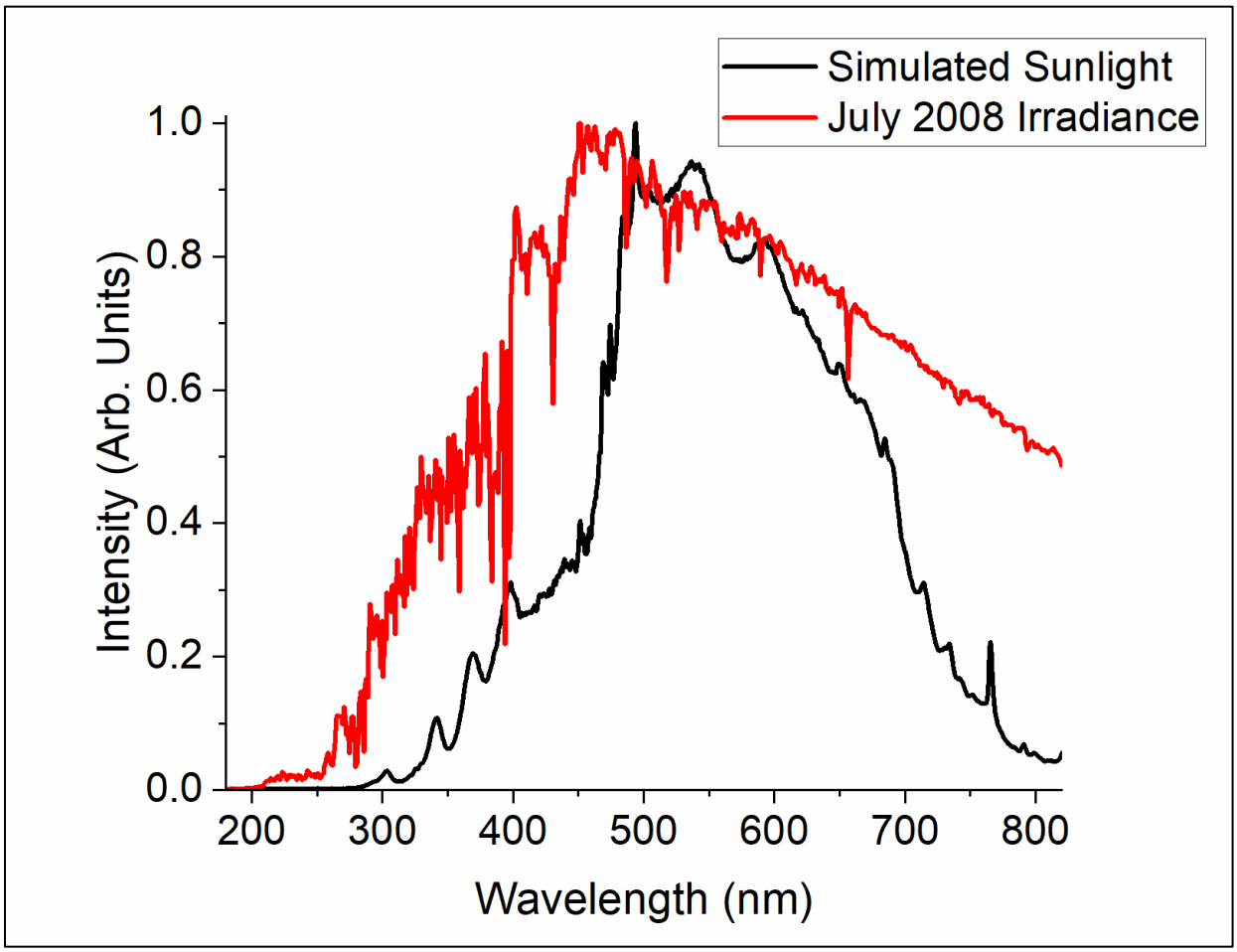

S1. Spectral output of the Oriel LCS-100 solar simulator compared to the spectral irradiance of a sunny day on July 1st, 2008.

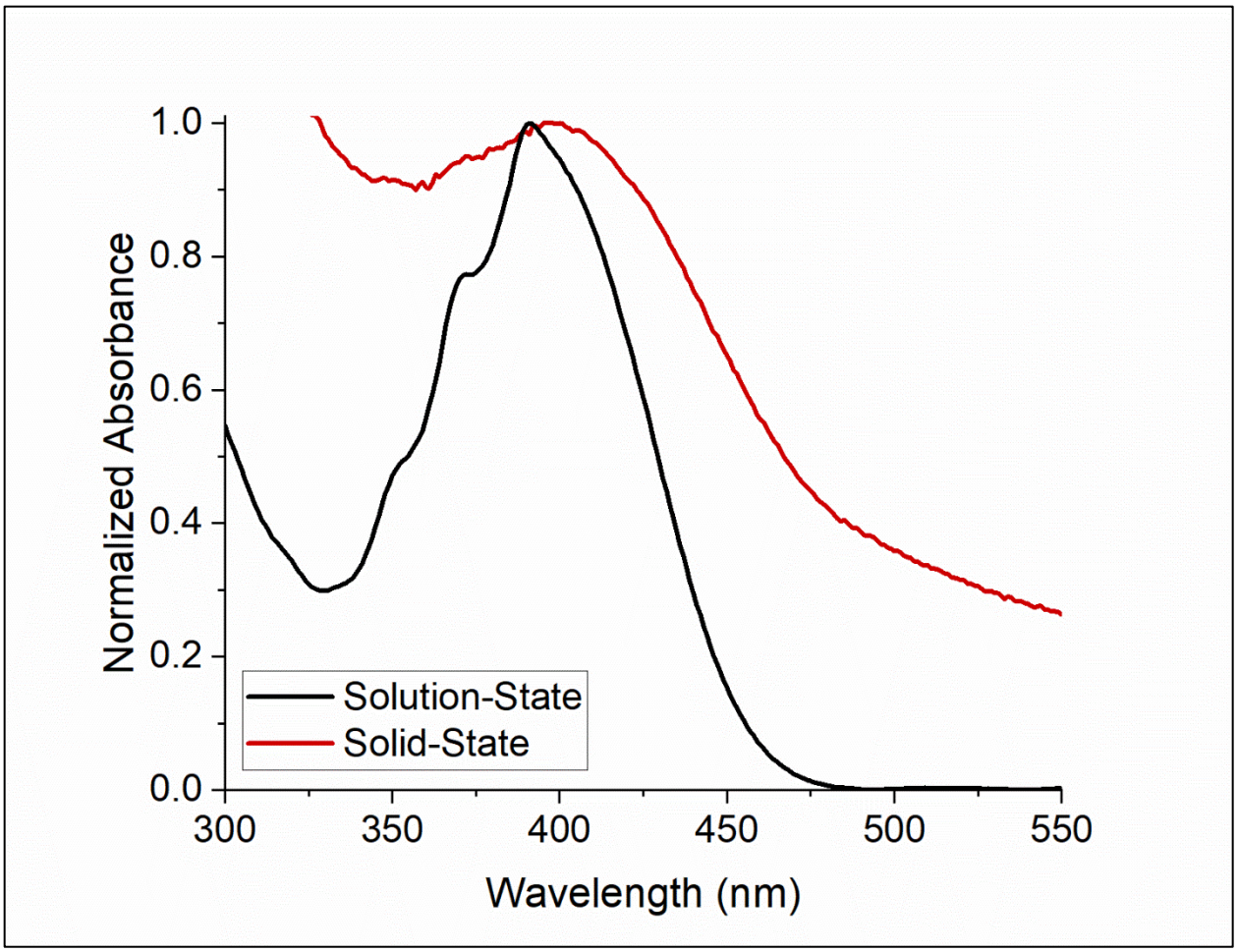

S2. UV-Visible absorption spectra of **C4-ATD** in DMF (black) compared to solid microwires filtered and spread onto a glass slide (red).

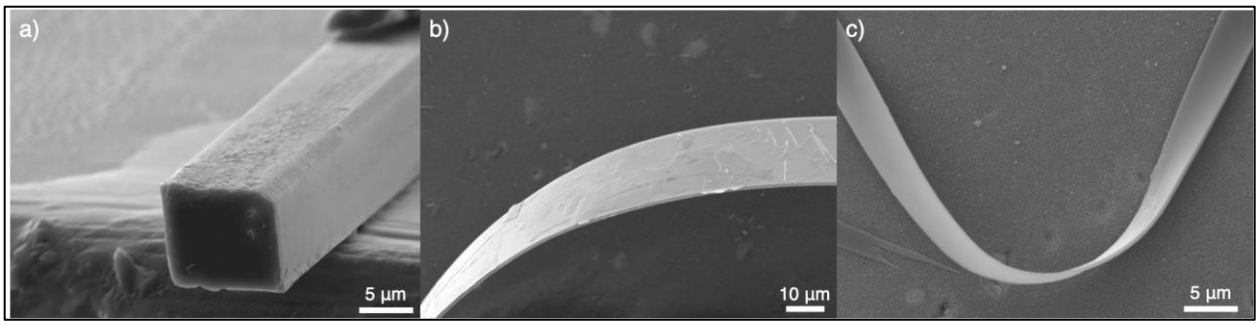

S3. SEM images showing the a) cross section of a **C4-ATD** microwire and the flexibility of **C4-ATD** microribbons (b-c).

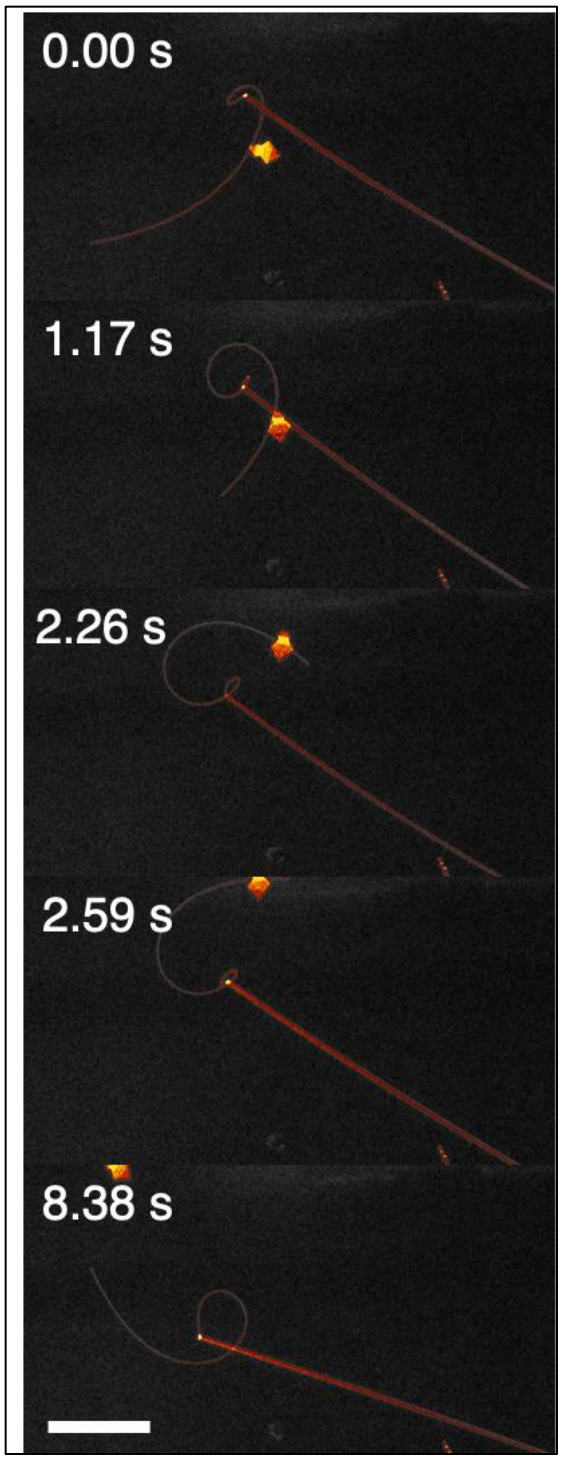

S4. Sequential microscopy images of **C4-ATD** showing cooperative behavior between a microwire fused to a microribbon under 405 nm light. Scale bar: 250 μm.

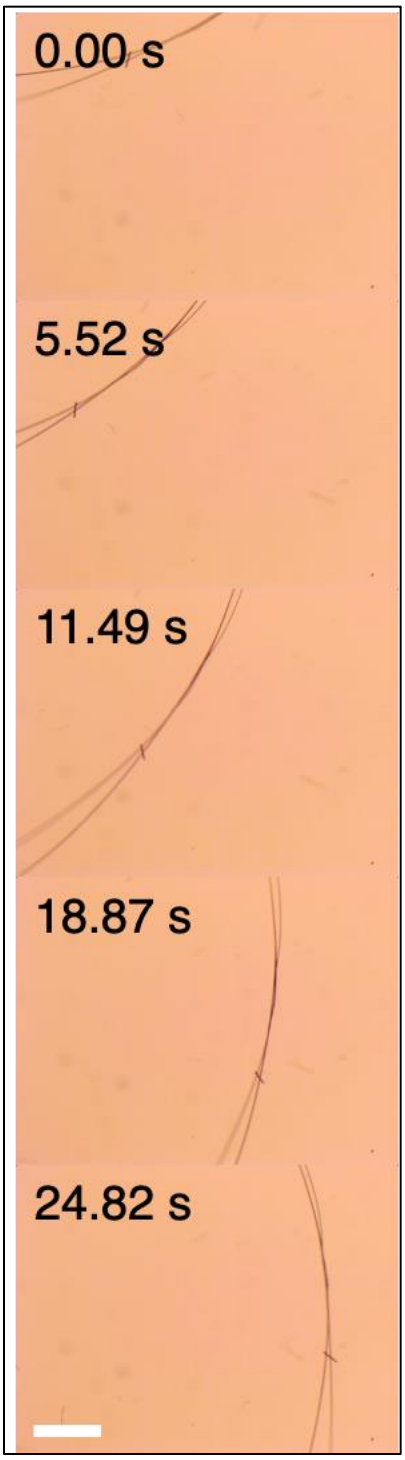

S5. Sequential microscopy images of **C4-ATD** showing two microwires "walking" together under 405 nm light. Scale bar: 25 μm.

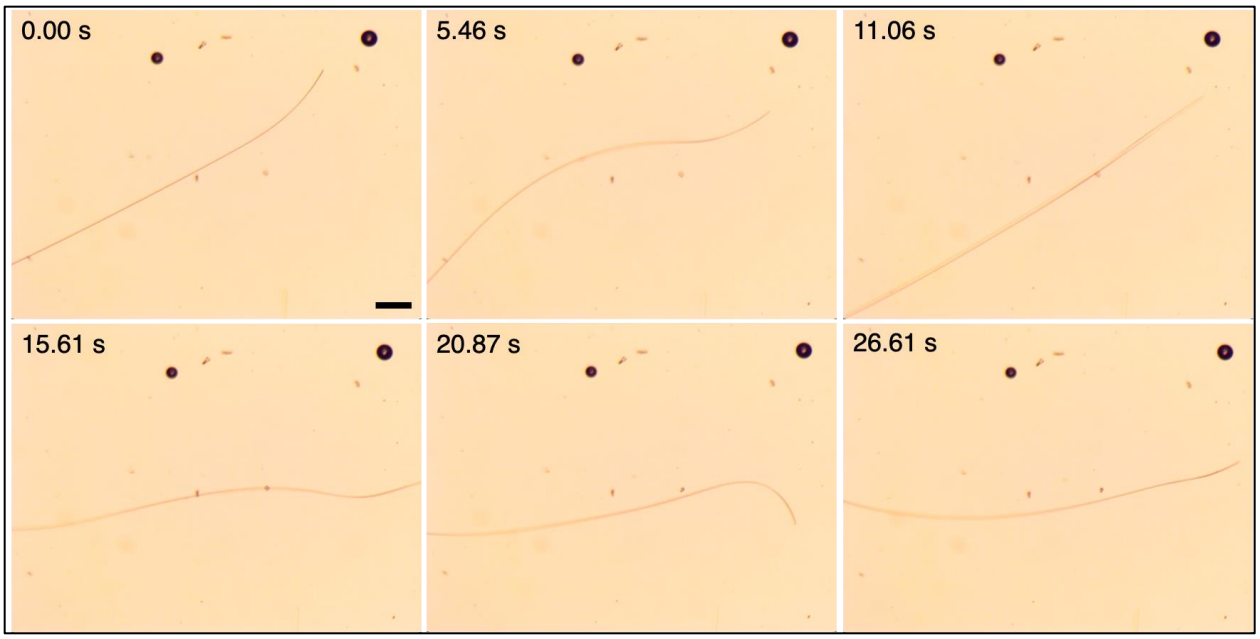

S6. Sequential microscopy images of **C4-ATD** showing random writhing of a microribbon under 405 nm light. Scale bar: 25 μm.

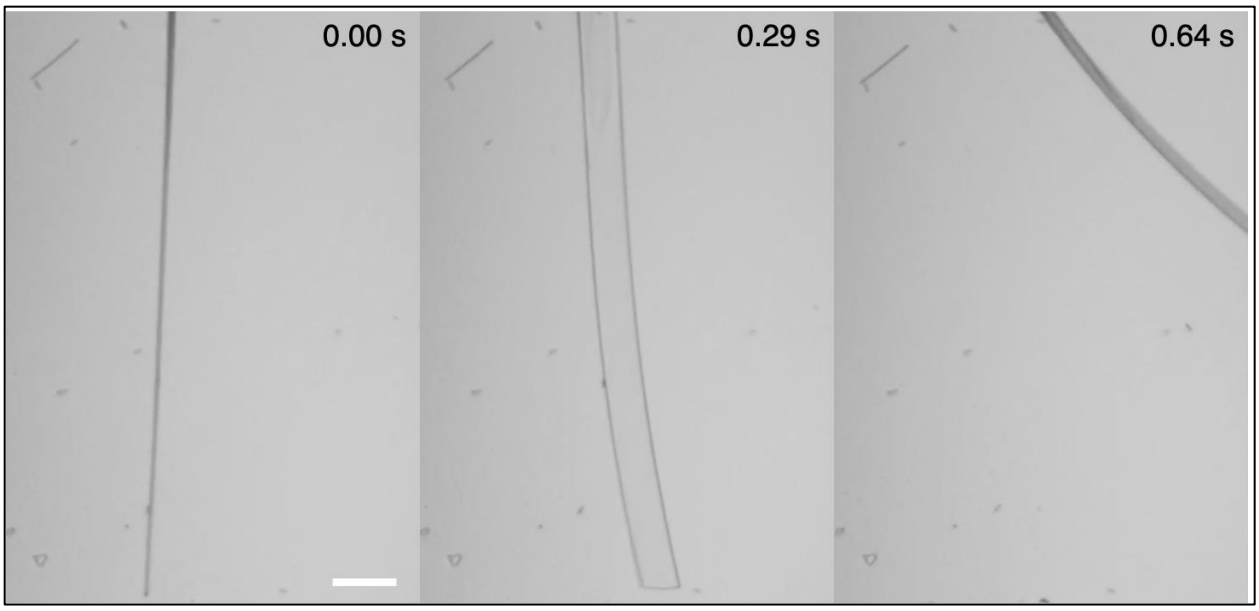

S7. Sequential microscopy images of **C4-ATD** showing dramatic flexing of a microribbon under 405 nm light. Scale bar: 100 μm.

Electronic Supplementary Information

Experimental section:

General:

All organic solvents employed in this study were of reagent grade, while spectroscopic grade solvents were used in their as-received form. Thin layer chromatography (TLC) was carried out on 5x2.5 cm silica gel GF254 plates pre-coated on an aluminum support. TLC spots were visualized under UV light at a wavelength of 254 nm or developed through chemical staining with potassium permanganate ($KMnO_4$). Reagents, including 9-anthraldehyde, thiazolidine-2,4-dione, K_2CO_3, and 1-bromobutane were procured from reputable suppliers, namely TCI America and Santa Cruz Biotechnology, and were used without further purification. Proton and carbon nuclear magnetic resonance (1H and 13C NMR) spectra were acquired at a temperature of 298 K using a JEOL spectrometer operating at 400 MHz. Proton chemical shifts were reported in parts per million (ppm, δ) with DMSO-d6 serving as the reference at δ 2.50 ppm. J values were expressed in hertz (Hz). Carbon chemical shifts were also reported in ppm (δ) with DMSO-d6 as the reference at δ 39.52 ppm. Complete proton decoupling was applied during 13C NMR experiments which was collected at 101 MHz. To enhance solubility of the analyte and prevent freezing of DMSO-d6, a 25% (v/v) mixture of DMSO-d6 in CCl4 was employed instead of pure DMSO-d6. Melting points (uncorrected) were determined using a 1101D Mel-Temp digital melting point apparatus. High-Performance Liquid Chromatography (HPLC) analysis was performed using a Shimadzu LC-20AD system, equipped with a Thermo Scientific general-purpose BDS Hypersil C18 column measuring 250 × 4.6 mm. The column temperature was maintained at a constant 35°C. A gradient mobile phase was employed, starting with 50% aqueous acetonitrile in water (pH = 2.5) and transitioning to 100% acetonitrile, with a flow rate of 1.5 mL/min. Detection was achieved at a wavelength of 254 nm. UV analysis of the E and Z photoisomer fractions was carried out using the Shimadzu LC-20AD system built-in UV-Vis cell. A 1.0 nm collection increment was used and a wavelength range for analysis was set between 200 and 600 nm. A solvent blank consisting of 90% CH_3CN / 10% water was collected before each measurement.

SYNTHESIS

(Z)-5-(anthracen-9-ylmethylene)thiazolidine-2,4-dione

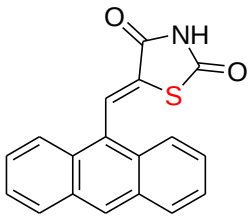

(**H-ATD**)

The following reaction Scheme-S1 was adopted

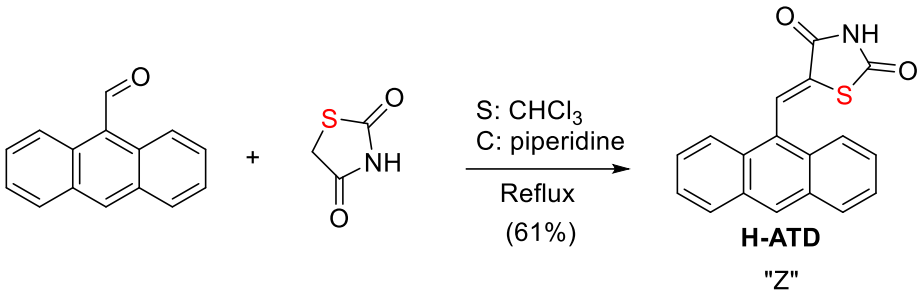

Scheme-S1: Synthesis of (Z)-5-(anthracen-9-ylmethylene)thiazolidine-2,4-dione (**H-ATD)**.

In a 100 mL round-bottom flask, 2.06 grams (10 mmol, 1 equivalent) of 9-anthraldehyde and 2.34 grams (20 mmol, 2 equivalents) of Thiazolidine-2,4-dione were dissolved in 30 mL of chloroform ($CHCl_3$), with the addition of 0.1 mL of piperidine as the catalyst. The reaction mixture was subjected to reflux for a period of 24 hours under an argon atmosphere. As the reaction progressed, a yellow-orange precipitate formed in the chloroform solution. Following the reflux, the organic solvent was removed via reduced pressure, resulting in the crude yellow colored solid product. Subsequently, this solid was suspended in 30 mL of methanol and subjected to sonication for 5 minutes. This step served to effectively wash away any excess Thiazolidine-2,4-dione and unreacted 9-anthraldehyde from the product. To isolate the pure (Z)-5-(anthracen-9-ylmethylene)thiazolidine-2,4-dione, suction filtration was employed, and the resulting solid was rinsed with cold methanol. Overall, the reaction yielded a yellow product, identified as pure (Z)-5-(anthracen-9-ylmethylene)thiazolidine-2,4-dione (**H-ATD**), with a total yield of 61%, equating to 2 grams.

1H NMR (400 MHz, DMSO-D_6) δ 12.51 (s, 1H, *N-H*), 8.62 (s, 1H), 8.56 (d, *J* = 0.7 Hz, 1H), 8.16 – 8.05 (m, 2H), 8.05 – 7.94 (m, 2H), 7.54 (dtd, *J* = 8.2, 6.5, 5.1 Hz, 4H). Figure-S1

13C NMR (101 MHz, DMSO-D6) δ 167.57, 166.29, 133.06, 131.22, 130.14, 129.38, 129.28, 128.48, 127.65, 126.98, 125.80, 125.31. Figure-S2

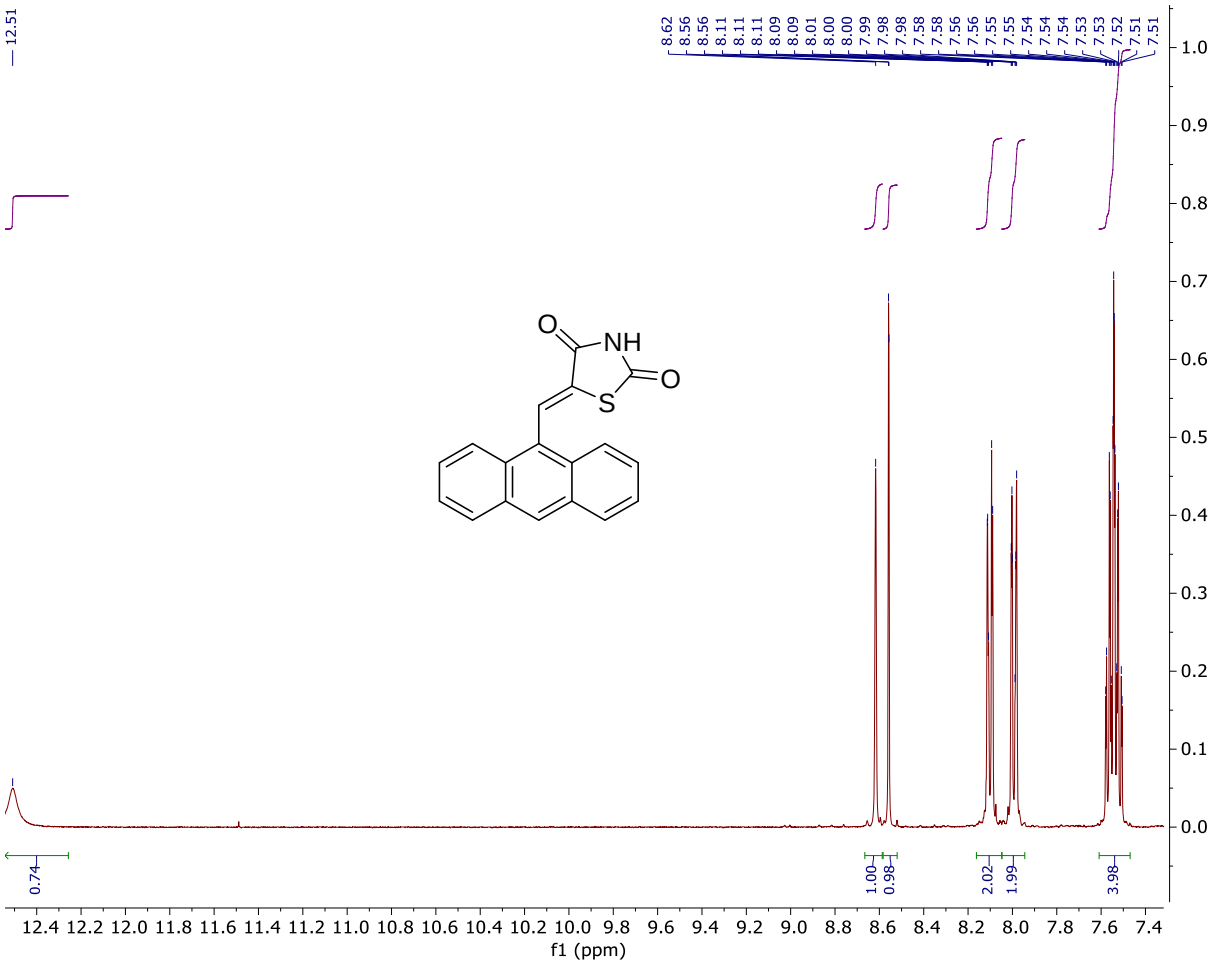

Figure-S1: 1H NMR of H-ATD in 25% DMSO-d6/ 75% CCl_4 (V/V)

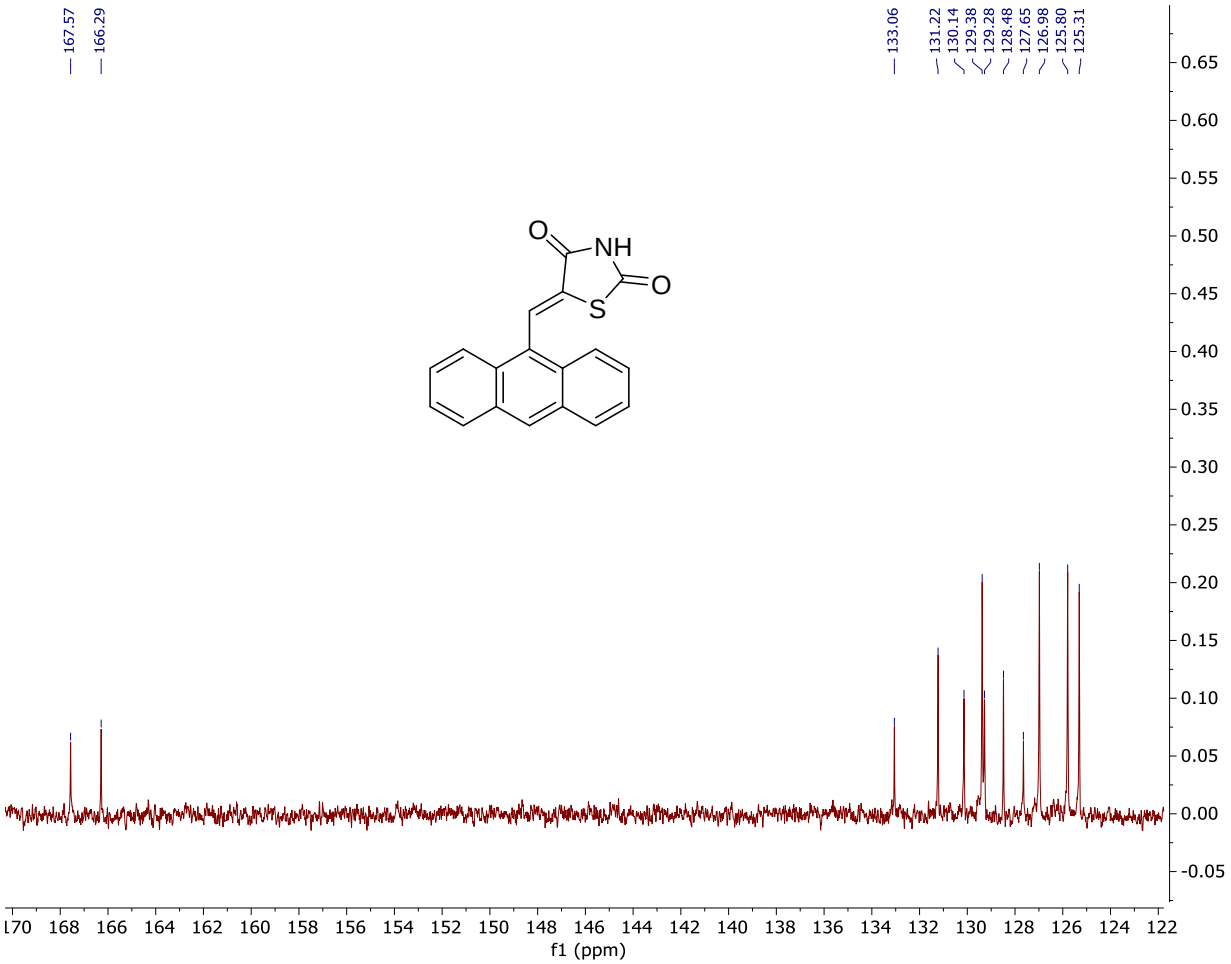

Figure-S2: 13C NMR of H-ATD in 25% DMSO-d6/ 75% CCl_4 (V/V)

(Z)-5-(anthracen-9-ylmethylene)-3-butylthiazolidine-2,4-dione

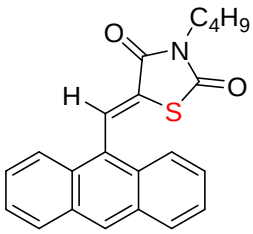

C4-ATD

The following reaction Scheme-S2 was used:

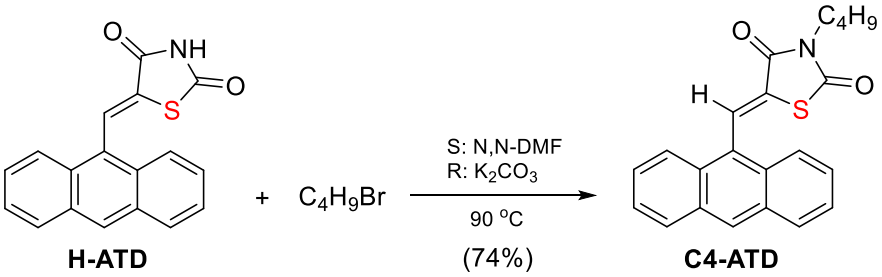

Scheme-S2: Synthesis of Z isomer of **C4-ATD**

In a 40 mL reaction vial, (Z)-5-(anthracen-9-ylmethylene)thiazolidine-2,4-dione (**H-ATD**) (0.5 grams, 1.6 mmol) was dissolved in 4 mL of anhydrous N,N-dimethylformamide (N,N-DMF). To this solution, an excess of potassium carbonate (1 gram, 7.1 mmol) and an excess of 1-bromobutane (0.25 mL) were added. The reaction mixture was stirred at 90°C for a brief duration (5 min) to ensure complete consumption of the reactants. The progression of the reaction was monitored via thin-layer chromatography (TLC) employing a mobile phase consisting of 75% hexane and 25% ethyl acetate. Subsequently, to isolate the product, 40 mL of water was introduced into the cooled reaction mixture, leading to the precipitation of the product **C4-ATD**. The mixture was stirred at room temperature for 10 minutes. The resulting crude yellow product was separated through suction filtration and then washed with cold methanol for purification. For further purification, the crude product was subjected to recrystallization using a boiling mixture of acetonitrile and water, yielding long, yellow, needle-like crystals (0.43 grams) with a yield of 74% and a melting point 140-142 °C.

1H NMR (400 MHz, DMSO-D6) δ 8.69 (s, 1H), 8.63 (s, 1H), 8.11 (dd, J = 7.2, 1.8 Hz, 2H), 8.05 – 7.95 (m, 2H), 7.62 – 7.47 (m, 4H), 3.72 (t, J = 7.3 Hz, 2H), 1.69 (dd, J = 8.5, 6.2 Hz, 2H), 1.52 – 1.33 (m, 2H), 1.02 (t, J = 7.3 Hz, 3H). Figure-S3

13C NMR (101 MHz, DMSO-D6) δ 166.67, 164.25, 131.02, 130.83, 130.27, 129.16, 129.03, 128.14, 126.89, 126.68, 125.44, 124.87, 41.31, 29.54, 19.66, 13.56. Figure-S4

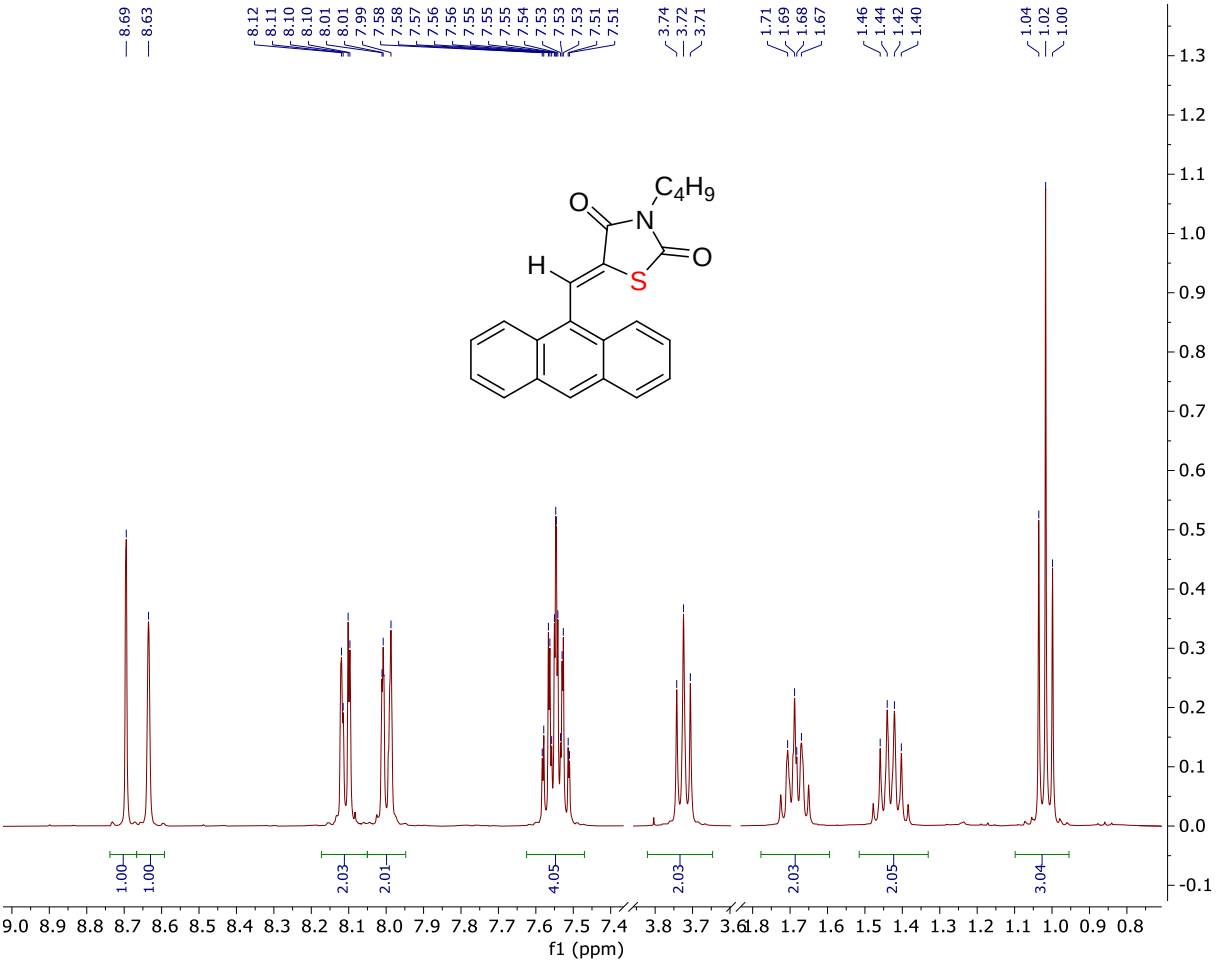

Figure-S3: 1H NMR of **C4-ATD** in 25% DMSO-d6/ 75% CCl_4 (V/V)

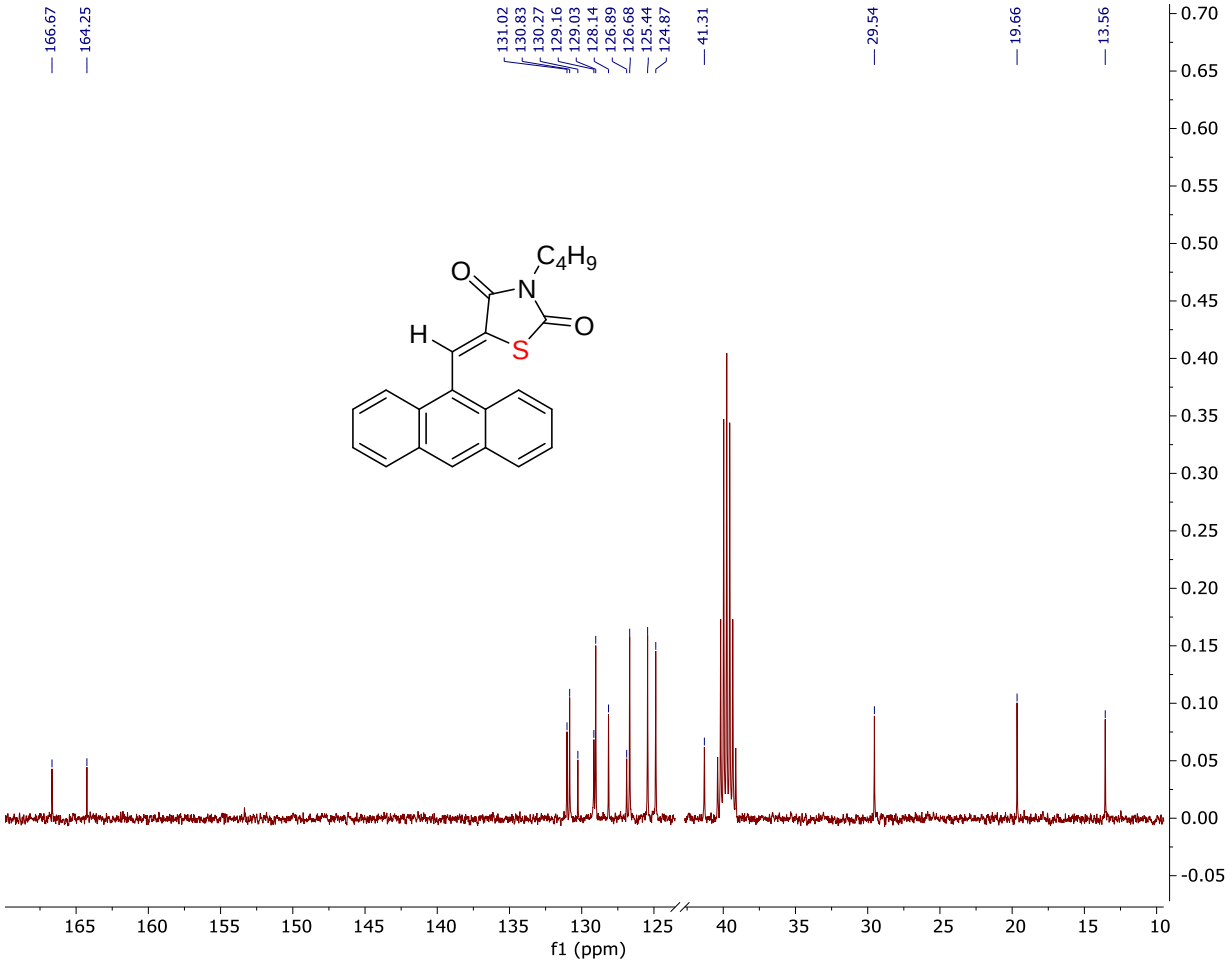

Figure-S4: 13C NMR of **C4-ATD** in 25% DMSO-d6/ 75% CCl_4 (V/V)

Growing crystalline microwires of Z **C4-ATD**:

The seeded growth method from aqueous solutions containing surfactants proved to be successful in engineering acicular crystal habits from photoreactive molecules. In the case of the present molecule, the use of aqueous surfactants played a crucial role in determining both the crystal structure and morphology.

A. *Preparation of the organic solution*: A concentrated organic solution of **C4-ATD** Z-isomer was prepared in N,N-dimethylformamide (DMF) with a concentration of 10 mg of the compound dissolved in every 250 microliters of DMF. Gentle heating was employed to facilitate the dissolution of the compound. The resulting organic solution was then set aside, away from ambient light and kept warm.
B. *Preparation of the **C4-ATD** crystal seeds*: In a 20 mL test tube, 300 mg of sodium dodecyl sulfate (SDS) and 8 mg of **C4-ATD** were combined. Ethanol (10 mL) was added and the mixture was gently heated until boiling to dissolve the SDS and **C4-ATD**, resulting in a yellow homogeneous solution. Subsequently, 10 mL of warm water was added to the test tube, and the mixture was gently boiled for a few seconds. After allowing the test tube and its contents to sit at room temperature in a dark place for 24 hours, long acicular crystals of **C4-ATD** with random thickness precipitated out of the solution. The seed crystals were collected by suction filtration, possessing the desired polymorph and suitable for the production of microwires.
C. *Preparation of the aqueous surfactant solution*: An aqueous solution of the surfactant mixture was prepared by dissolving SDS and diphenylcyanoacrylate (DPC) in 40 mL of water. The mixture was warmed to 45 degrees Celsius before rapidly injecting 200 microliters of the organic solution prepared in A. This resulted in the formation of a yellow, turbid, and oily suspension.
D. *Fabrication of **C4-ATD** microwires*: Approximately two milligrams of the seed crystals prepared in B were resuspended in the yellowish aqueous surfactant solution from C and kept at 45 ^{o}C for a couple of days. Consequently, long acicular microwires of the photomechanically active polymorph of **C4-ATD** precipitated out of the aqueous solution.

HPLC, UV-Vis and H NMR analysis of the E C4-ATD photisomer:

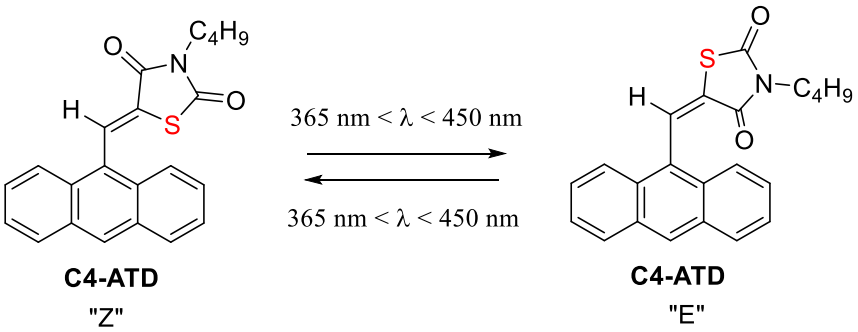

Scheme-S3: Photoisomerization of **C4-ATD** in solution upon UV or visible light irradiation.

To initiate the experiment, (Z)-5-(anthracen-9-ylmethylene)-3-butylthiazolidine-2,4-dione (10 mg) was dissolved in 50 mL of (HPLC)-grade acetonitrile, followed by thorough degassing using argon (Agon). Subsequently, the degassed solution was subjected to irradiation with 405 nm light for several hours. After the irradiation period, the reaction mixture was analyzed using HPLC (Figure-S5a, b). Notably, both isomers were found to be present in the reaction mixture in an approximately equimolar ratio. For further characterization, UV-Vis analysis of each photoproduct peak was performed at their respective retention times, allowing accurate identification and quantification of each isomer. UV-Vis of the E and Z fraction were collected in a solvent that is 90% acetonitrile and 10% water.

In another experiment, a sample of C4-ATD was partially irradiated with 365 nm and analyzed using H NMR confirming the photoisomerization chemistry. Figure-S7

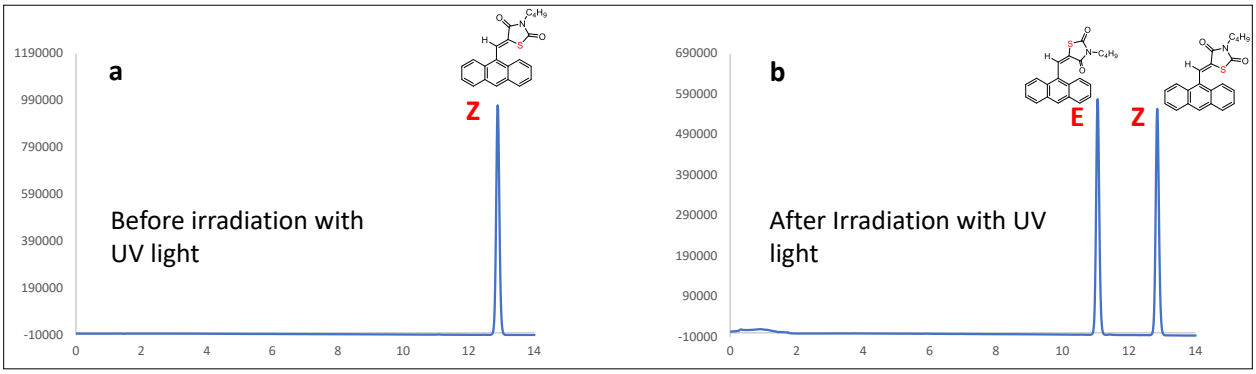

Figure-S5: HPLC analysis of **C4-ATD**. a) HPLC chromatogram of pure Z isomer of C4-ATD dissolved in acetonitrile. b) HPLC chromatogram of Z and E isomers of C4-ATD after irradiation with 405 nm in acetonitrile. The mixture reached a steady state after several hours. The E isomer elutes out of the column (11.05 min) around two minutes before the Z isomer (12.85 min) at a flow rate of 1.5 ml/min. This provides us enough time to analyze the UV-Vis spectrum of each fraction.

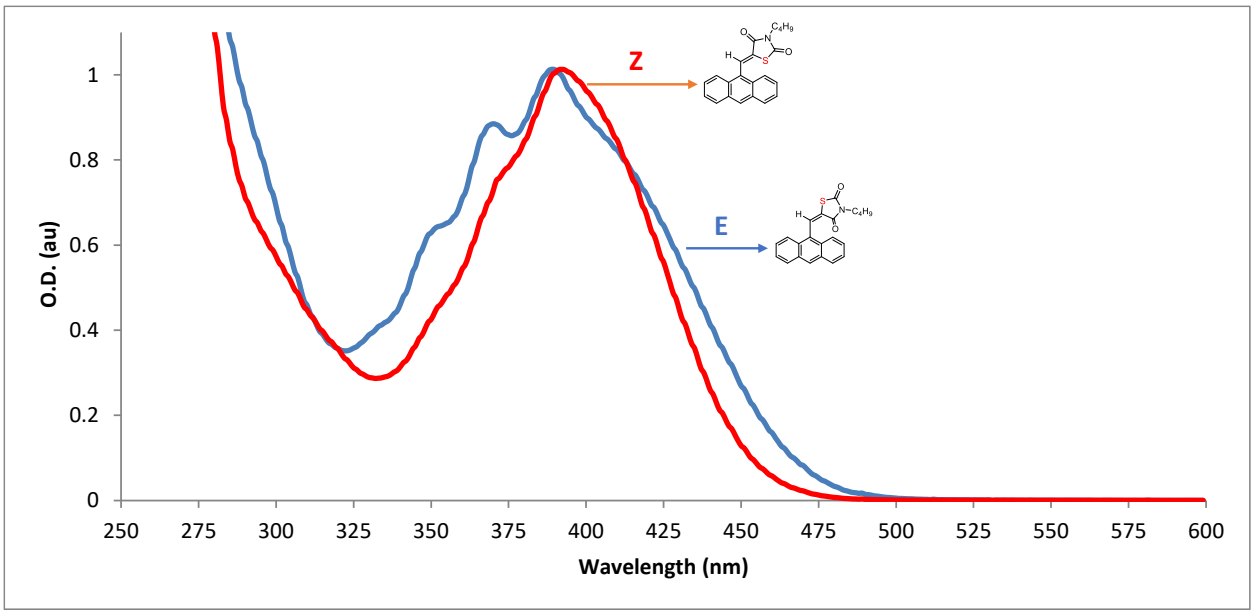

Figure-S6: Normalized UV-Vis spectrum of the E and Z **C4-ATD** photoisomers in 90% CH_3CN/ 10% H_2O. Notice the structured anthracene-like absorption bands in the E isomer.

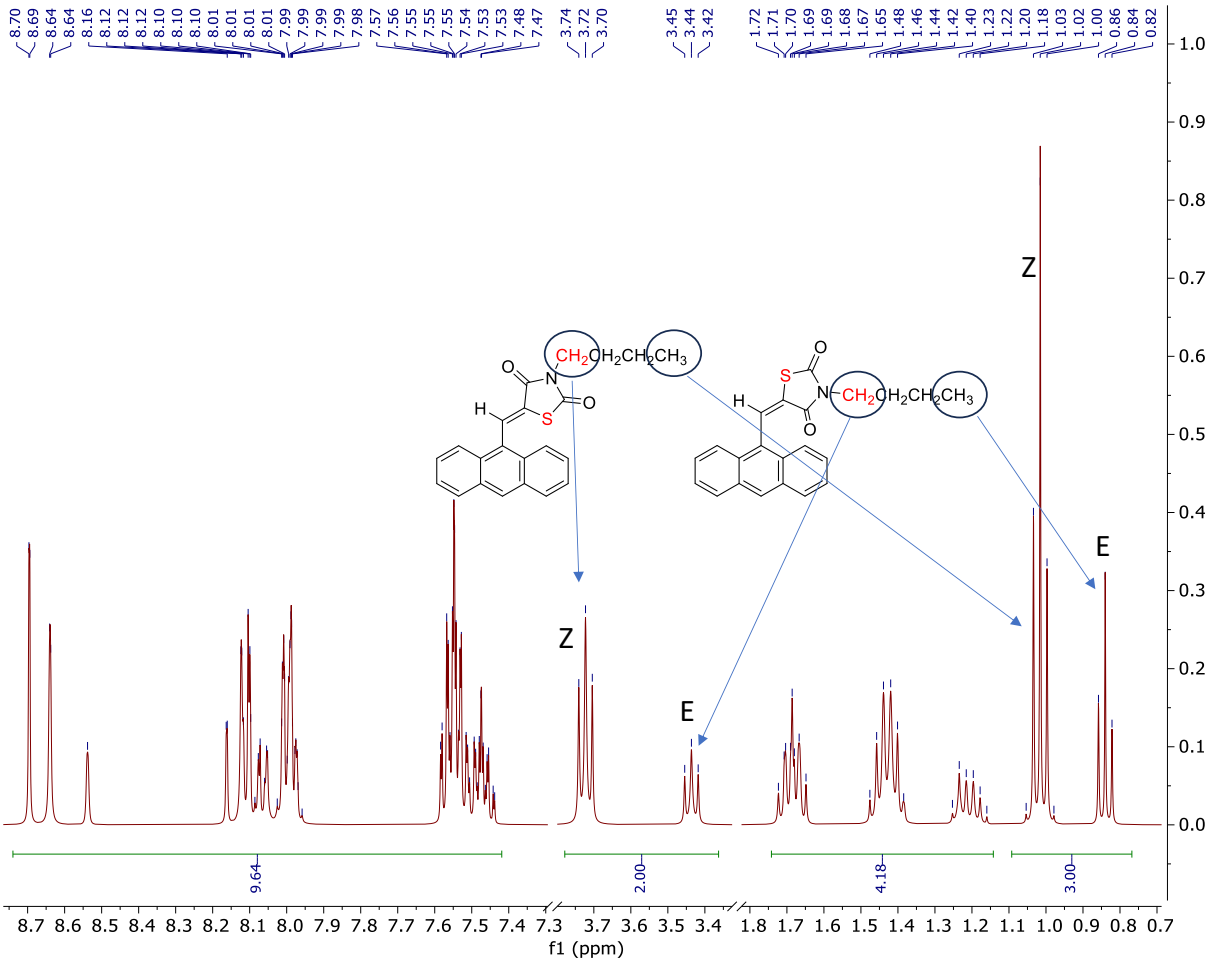

Figure-S7: H NMR of a partially irradiated solution of Z C4-ATD in acetonitrile using 365 nm light. The formation of the E isomer is evident from the chemical shift of the butyl protons. The

Optical Microscopy Measurements:

To view the microcrystals, the (Z)-**C4-ATD** suspension was incubated at 45 ºC in a convection oven for several hours to solubilize any residual surfactant in solution. The suspension was then taken out of the oven and several drops were deposited onto a clean glass slide. A coverslip was then placed on top to reduce the rate of water evaporation. For microscopy images of static crystals, a Leica DM2700 M microscope (equipped with a Leica MC120 HD digital camera) was used. For dynamic

photomechanical motions, an Olympus IX50 inverted fluorescence microscope equipped with an AmScope MU203-BI digital camera was used. Light from an Olympus U-LH100HG 100W Hg lamp was filtered through an Olympus U-MNV fluorescence filter cube to provide the 405 nm excitation source. An Oriel LCS-100 Small Area Sol1A solar simulator was used for the sunlight measurements.

Optical Spectroscopy Measurements:

All measurements were collected using a Cary 60 UV-Vis Spectrophotometer. Solution-state measurements were conducted in DMF with a 1 cm path length quartz cuvette. Solid-state measurements were performed by first filtering the "reactive" rod-like polymorph onto a blank anodic aluminum oxide (AAO) template (Whatman Anodisc inorganic filter membrane diameter 12.7 mm, nominal pore size ~ 0.2μm). The crystals were then thoroughly washed with H_2O and spread onto a clean glass slide using a hypodermic needle.

Scanning Electron Microscopy Measurements:

Several drops of the active (Z)-**C4-ATD** suspension were deposited onto a blank AAO template, dried via vacuum filtration, and washed with H_2O. The template was then left to air-dry overnight in the dark. After drying, the AAO template was adhered onto an SEM stub using carbon tape and sputter coated with Au for 60 seconds using a Cressington 108 Auto. Images were collected on a TESCAN Vega3 SBH with a 10 kV electron beam in high vacuum at $<10^{-3}$ Pa.

Powder X-Ray Diffraction Measurements:

Several drops of the active (Z)-**C4-ATD** suspension were deposited onto a blank AAO template, dried via vacuum filtration, and washed thoroughly with H_2O. The template was then left to air-dry overnight in the dark. All PXRD measurements were collected using a PANalytical Empyrean Series 2 diffractometer with CuK_α radiation (λ = 1.5418 Å, 45 kV/40 mA power). The following slit sizes were used: incident divergence (1/2º), incident anti-scatter (1º), and diffracted anti-scatter (P8.0). The sample stage was set to spin with a revolution time of 2 seconds and step size of 0.0131 degrees.

Single-Crystal X-Ray Structural Determination Measurements:

A colorless crystal (plate, approximate dimensions 0.14 × 0.09 × 0.04 mm^3) was placed onto the tip of a MiTeGen pin and mounted on a Bruker Venture D8 diffractometer equipped with a PhotonIII detector at 100.00 K. The data collection was carried out using Cu Kα radiation (λ = 1.54178 Å, IμS micro-source) with a frame time of 8 seconds and a detector distance of 40 mm. A collection strategy was calculated and complete data to a resolution of 0.84 Å were collected. The frames were integrated with the Bruker SAINT[1] software package using a narrow-frame algorithm to 0.84 Å resolution. Data were corrected for absorption effects using the multi-scan method (SADABS).[2] Please refer to Table 1 for additional crystal and refinement information. Data suffers from weak peak intensity, which decreases dramatically at high angles.

The space group P $2_1/n$ was determined based on intensity statistics and systematic absences. The structure was solved using the SHELX suite of programs[3] and refined using full-matrix least-squares on F^2 within the OLEX2 suite.[4] An intrinsic phasing

solution was calculated, which provided non-hydrogen atoms from the E-map. Full-matrix least squares / difference Fourier cycles were performed. All non-hydrogen atoms were refined with anisotropic displacement parameters. The hydrogen atoms were placed in ideal positions and refined as riding atoms with relative isotropic displacement parameters. The final full matrix least squares refinement converged to R1 = 0.1125 and wR2 = 0.2695 (F^2, all data). The goodness-of-fit was 1.092. On the basis of the final model, the calculated density was 1.374 g/cm^3 and F(000), 760 e$^-$.

Table S1. Crystal data and structure refinement for (Z)-**C4-ATD** [Active Polymorph]

Empirical formula	C22 H19 N O2 S	
Formula weight	361.44	
Crystal color, shape, size	colorless plate, 0.14 × 0.09 × 0.04 mm^3	
Temperature	100.00 K	
Wavelength	1.54178 Å	
Crystal system, space group	Monoclinic, P $2_1/n$	
Unit cell dimensions	a = 5.1897(9) Å	α = 90°.
	b = 19.070(3) Å	β = 97.607(12)°.
	c = 17.808(3) Å	γ = 90°.
Volume	1746.8(5) Å^3	
Z	4	
Density (calculated)	1.374 g/cm^3	
Absorption coefficient	1.773 mm^{-1}	
F(000)	760	
Data collection		
Diffractometer	Bruker D8 Venture	
Theta range for data collection	4.637 to 66.255°.	
Index ranges	-5<=h<=5, -22<=k<=20, -16<=l<=21	
Reflections collected	12273	
Independent reflections	2883 [Rint = 0.1913]	
Observed Reflections	1474	
Completeness to theta = 66.255°	94.3 %	
Solution and Refinement		
Absorption correction	Semi-empirical from equivalents	
Max. and min. transmission	0.7528 and 0.4770	
Solution	Intrinsic methods	
Refinement method	Full-matrix least-squares on F^2	
Weighting scheme	w = [σ^2Fo^2+ AP^2+ BP]$^{-1}$, with	

	P = (Fo^2+ 2 Fc^2)/3, A = 0.105, B = 2.51
Data / restraints / parameters	2883 / 0 / 236
Goodness-of-fit on F^2	1.092
Final R indices [I>2σ(I)]	R1 = 0.1125, wR2 = 0.2271
R indices (all data)	R1 = 0.1990, wR2 = 0.2695
Largest diff. peak and hole	0.678 and -0.567 e.$Å^{-3}$

A yellow crystal (block, approximate dimensions 0.48 × 0.29 × 0.17 mm^3) was placed onto the tip of a MiTeGen pin and mounted on a Bruker Venture D8 diffractometer equipped with a PhotonIII detector at 100.00 K. The data collection was carried out using Mo Ka radiation (l = 0.71073 Å, ImS micro-source) with a frame time of 2 seconds and a detector distance of 40 mm. A collection strategy was calculated and complete data to a resolution of 0.77 Å collected. The frames were integrated with the Bruker SAINT[1] software package using a narrow-frame algorithm to 0.77 Å resolution. Data were corrected for absorption effects using the multi-scan method (SADABS).[2] Please refer to Table 1 for additional crystal and refinement information.

The space group P $2_1/c$ was determined based on intensity statistics and systematic absences. The structure was solved using the SHELX suite of programs[3] and refined using full-matrix least-squares on F^2 within the OLEX2 suite.[4] An intrinsic phasing solution was calculated, which provided most non-hydrogen atoms from the E-map. Full-matrix least squares / difference Fourier cycles were performed, which located the remaining non-hydrogen atoms. All non-hydrogen atoms were refined with anisotropic

displacement parameters. The hydrogen atoms were placed in ideal positions and refined as riding atoms with relative isotropic displacement parameters. The final full matrix least squares refinement converged to R1 = 0.0353 and wR2 = 0.0955 (F^2, all data). The goodness-of-fit was 1.078. On the basis of the final model, the calculated density was 1.344 g/cm^3 and F(000), 760 e^-.

Table S2. Crystal data and structure refinement for (Z)-**C4-ATD** [Inactive Polymorph]

Empirical formula	C22 H19 N O2 S	
Formula weight	361.44	
Crystal color, shape, size	yellow block, 0.48 × 0.29 × 0.17 mm^3	
Temperature	100.00 K	
Wavelength	0.71073 Å	
Crystal system, space group	Monoclinic, P 1 21/c 1	
Unit cell dimensions	a = 13.1134(6) Å	a = 90°.
	b = 12.9052(6) Å	b = 111.956(2)°.
	c = 11.3799(6) Å	g = 90°.
Volume	1786.15(15) $Å^3$	
Z	4	
Density (calculated)	1.344 g/cm^3	
Absorption coefficient	0.197 mm^{-1}	
F(000)	760	
Data collection		
Diffractometer	Bruker D8 Venture	
Theta range for data collection	1.674 to 27.540°.	
Index ranges	-17<=h<=17, -16<=k<=16, -14<=l<=14	
Reflections collected	69618	
Independent reflections	4117 [Rint = 0.0755]	
Observed Reflections	3621	
Completeness to theta = 25.242°	99.9 %	
Solution and Refinement		
Absorption correction	Semi-empirical from equivalents	
Max. and min. transmission	0.7456 and 0.6640	
Solution	Intrinsic methods	
Refinement method	Full-matrix least-squares on F^2	

Weighting scheme	$w = [s^2Fo^2 + AP^2 + BP]^{-1}$, with $P = (Fo^2 + 2\,Fc^2)/3$, A = 0.041, B = 0.92
Data / restraints / parameters	4117 / 0 / 236
Goodness-of-fit on F^2	1.078
Final R indices [I>2s(I)]	R1 = 0.0353, wR2 = 0.0893
R indices (all data)	R1 = 0.0414, wR2 = 0.0955
Largest diff. peak and hole	0.447 and -0.344 e.$Å^{-3}$

[1]SAINT, V8.30A, Bruker Analytical X-Ray Systems, Madison, WI, 2012.

[2]SADABS, 2.03, Bruker Analytical X-Ray Systems, Madison, WI, 2016.

[3]G. M. Sheldrick, Acta Cryst. A64, 112 - 122 (2008). Sheldrick, G.M. (2015). Acta Cryst. A71, 3-8.

[4]O. V. Dolomanov, L. J. Bourhis, R. J. Gildea, J. A. K. Howard and H. Puschmann, J. Appl. Crystallogr., 2009, 42, 339–341.

Transition Dipole Moment Calculations:

The transition dipole moments for (Z)-**C4-ATD** and (E)-**C4-ATD** were calculated using Gaussian 16 at the TD-DFT CAM-B3LYP/6-311++G** level of theory from ab-initio DFT optimized structures calculated at the same level of theory. The detailed output information can be found in Supporting Information Tables S3-S6.

Table S3. Cartesian coordinates of (Z)-**C4-ATD** used for the TD-DFT calculation.

Atom	X (Å)	Y (Å)	Z (Å)
C	4.3752	-0.67929	0.47164
N	2.94816	-0.70974	0.15565
C	2.00684	-0.10086	0.96837
C	0.64108	-0.26182	0.39077
C	-0.42398	0.28234	0.97631
C	-1.81802	0.24284	0.49494
C	-2.52319	-0.97012	0.38996
C	-3.8733	-0.95679	-0.09142
C	-4.47249	0.25182	-0.42368
C	-3.79669	1.46052	-0.29394
C	-4.4199	2.70158	-0.62335
C	-3.75014	3.8759	-0.49793
C	-2.40483	3.88106	-0.04024
C	-1.77388	2.7191	0.27649
C	-2.44539	1.46173	0.17394
H	-0.74281	2.7432	0.60467
H	-1.87714	4.82296	0.04975
H	-4.23323	4.81212	-0.74968
H	-5.44429	2.68426	-0.97796
H	-5.49495	0.25321	-0.78659
C	-4.58484	-2.19027	-0.2056
C	-4.01099	-3.36537	0.1548
C	-2.68403	-3.37959	0.6656
C	-1.96951	-2.23009	0.7801
H	-0.96748	-2.26057	1.18455
H	-2.24222	-4.32031	0.97131
H	-4.56057	-4.29453	0.0661
H	-5.60111	-2.16287	-0.58217
H	-0.21095	0.84765	1.88055
S	0.70493	-1.16551	-1.12311
C	2.48666	-1.31499	-1.00073

O	3.16833	-1.87247	-1.81226
O	2.27428	0.47696	1.99324
C	5.07999	0.52995	-0.1304
C	6.56703	0.55079	0.20917
C	7.28811	1.75626	-0.38388
H	7.20802	1.76552	-1.47391
H	8.34962	1.74986	-0.12861
H	6.86211	2.69169	-0.01211
H	7.03422	-0.37061	-0.15458
H	6.68995	0.54952	1.29752
H	4.60304	1.44173	0.24204
H	4.94925	0.51511	-1.21675
H	4.80672	-1.60628	0.0937
H	4.4527	-0.66935	1.55907

Table S4. Cartesian coordinates of (E)-**C4-ATD** used for the TD-DFT calculation.

Atom	X (Å)	Y (Å)	Z (Å)
C	-3.58205	-0.6453	-0.78692
N	-2.67161	-0.56118	0.35413
C	-1.30234	-0.40389	0.17657
C	-0.61701	-0.31319	1.50065
C	0.68862	-0.13055	1.69315
C	1.74858	-0.05021	0.66073
C	2.37603	1.1873	0.4461
C	3.44717	1.28281	-0.49726
C	3.8546	0.14441	-1.18296
C	3.25168	-1.08928	-0.96617
C	3.68533	-2.25754	-1.66418
C	3.10711	-3.46386	-1.43811
C	2.05364	-3.57943	-0.49019
C	1.60821	-2.49095	0.18946
C	2.18048	-1.19862	-0.02223
H	0.80774	-2.59933	0.90875
H	1.60421	-4.54878	-0.31049
H	3.44505	-4.34315	-1.97298
H	4.4929	-2.1567	-2.38053
H	4.66487	0.21905	-1.90058
C	4.07132	2.54869	-0.712
C	3.66601	3.65384	-0.03558
C	2.59884	3.56408	0.89942

C	1.97413	2.37842	1.12671
H	1.14936	2.33316	1.82685
H	2.27845	4.45382	1.42817
H	4.14801	4.60869	-0.20685
H	4.88006	2.60714	-1.43179
H	1.02664	-0.0131	2.72148
S	-1.80268	-0.42446	2.81331
C	-3.15222	-0.58545	1.64905
O	-4.30097	-0.70314	1.96684
O	-0.77788	-0.3432	-0.90515
C	-4.07559	0.72309	-1.24011
C	-5.01898	0.62194	-2.43456
C	-5.52109	1.98322	-2.90318
H	-6.0663	2.49682	-2.10714
H	-6.19368	1.88639	-3.75774
H	-4.69036	2.62642	-3.2046
H	-5.87217	-0.01172	-2.16964
H	-4.50496	0.11741	-3.25965
H	-3.21304	1.34332	-1.50204
H	-4.58718	1.21263	-0.40564
H	-4.41666	-1.27762	-0.48398
H	-3.03279	-1.14126	-1.58748

Table S5. Ground to excited state transition electric dipole moments for (Z)-**C4-ATD** from the TD-DFT Calculations.

State	X	Y	Z	Dip. S.	Osc.
1	1.6438	-0.1693	0.21	2.7747	0.2281
2	0.1863	0.0516	-0.1287	0.0539	0.0053
3	0.2173	-0.1917	-0.1134	0.0968	0.0096

Dipole moment (field-independent basis, Debye):

X	Y	Z	Tot
-1.6702	0.9066	0.4472	1.9522

Table S6. Ground to excited state transition electric dipole moments for (E)-**C4-ATD** from the TD-DFT Calculations.

State	X	Y	Z	Dip. S.	Osc.
1	1.2693	0.1257	-0.5579	1.938	0.1564
2	0.3264	0.0046	-0.4293	0.2909	0.0264

3	-0.0246	-0.1752	-0.0557	0.0344	0.0034

Dipole moment (field-independent basis, Debye):

X	Y	Z	Tot
1.7757	0.4600	-1.1306	2.1407

References:

(1) Schliwa, M.; Woehlke, G. Molecular Motors. *Nature* **2003**, *422* (6933), 759–765. https://doi.org/10.1038/nature01601.

(2) Aprahamian, I. The Future of Molecular Machines. *ACS Cent. Sci.* **2020**, *6* (3), 347–358. https://doi.org/10.1021/acscentsci.0c00064.

(3) Kassem, S.; Van Leeuwen, T.; Lubbe, A. S.; Wilson, M. R.; Feringa, B. L.; Leigh, D. A. Artificial Molecular Motors. *Chem. Soc. Rev.* **2017**, *46* (9), 2592–2621. https://doi.org/10.1039/c7cs00245a.

(4) Al-Kaysi, R. O.; Bardeen, C. J. Reversible Photoinduced Shape Changes of Crystalline Organic Nanorods. *Adv. Mater.* **2007**, *19* (9), 1276–1280. https://doi.org/10.1002/adma.200602741.

(5) Al-Kaysi, R. O.; Müller, A. M.; Bardeen, C. J. Photochemically Driven Shape

Changes of Crystalline Organic Nanorods. *J. Am. Chem. Soc.* **2006**, *128* (50), 15938–15939. https://doi.org/10.1021/ja064535p.

(6) Cook, C. J.; Li, W.; Lui, B. F.; Gately, T. J.; Al-Kaysi, R. O.; Mueller, L. J.; Bardeen, C. J.; Beran, G. J. O. A Theoretical Framework for the Design of Molecular Crystal Engines. *Chem. Sci.* **2022**, *14* (4), 937–949. https://doi.org/10.1039/d2sc05549j.

(7) Zhu, L.; Tong, F.; Salinas, C.; Al-Muhanna, M.; Tham, F.; Kisailus, D.; Al-Kaysi, R.; Bardeen, C. Light Powered Ratchet. In *Abstracts of Papers, 251st ACS National Meeting & Exposition, San Diego, CA, United States*; American Chemical Society Washington, D. C, 2016; p ORGN-645.

(8) Awad, W. M.; Davies, D. W.; Kitagawa, D.; Mahmoud Halabi, J.; Al-Handawi, M. B.; Tahir, I.; Tong, F.; Campillo-Alvarado, G.; Shtukenberg, A. G.; Alkhidir, T.; Hagiwara, Y.; Almehairbi, M.; Lan, L.; Hasebe, S.; Karothu, D. P.; Mohamed, S.; Koshima, H.; Kobatake, S.; Diao, Y.; Chandrasekar, R.; Zhang, H.; Sun, C. C.; Bardeen, C.; Al-Kaysi, R. O.; Kahr, B.; Naumov, P. Mechanical Properties and Peculiarities of Molecular Crystals. *Chem. Soc. Rev.* **2023**, *52* (9), 3098–3169. https://doi.org/10.1039/d2cs00481j.

(9) Tong, F.; Kitagawa, D.; Bushnak, I.; Al-Kaysi, R. O.; Bardeen, C. J. Light-Powered Autonomous Flagella-Like Motion of Molecular Crystal Microwires. *Angew. Chemie - Int. Ed.* **2021**, *60* (5), 2414–2423. https://doi.org/10.1002/anie.202012417.

(10) Zhu, L.; Tong, F.; Zaghloul, N.; Baz, O.; Bardeen, C. J.; Al-Kaysi, R. O. Characterization of a P-Type Photomechanical Molecular Crystal Based on the: E

→ Z Photoisomerization of 9-Divinylanthracene Malonitrile. *J. Mater. Chem. C* **2016**, *4* (35), 8245–8252. https://doi.org/10.1039/c6tc02517j.

(11) Irie, M.; Fukaminato, T.; Matsuda, K.; Kobatake, S. Photochromism of Diarylethene Molecules and Crystals: Memories, Switches, and Actuators. *Chem. Rev.* **2014**, *114* (24), 12174–12277. https://doi.org/10.1021/cr500249p.

(12) van Beurden, K.; de Koning, S.; Molendijk, D.; van Schijndel, J. The Knoevenagel Reaction: A Review of the Unfinished Treasure Map to Forming Carbon–Carbon Bonds. *Green Chem. Lett. Rev.* **2020**, *13* (4), 85–100. https://doi.org/10.1080/17518253.2020.1851398.

(13) Gandini, A.; Bartolini, M.; Tedesco, D.; Martinez-Gonzalez, L.; Roca, C.; Campillo, N. E.; Zaldivar-Diez, J.; Perez, C.; Zuccheri, G.; Miti, A.; Feoli, A.; Castellano, S.; Petralla, S.; Monti, B.; Rossi, M.; Moda, F.; Legname, G.; Martinez, A.; Bolognesi, M. L. Tau-Centric Multitarget Approach for Alzheimer's Disease: Development of First-in-Class Dual Glycogen Synthase Kinase 3β and Tau-Aggregation Inhibitors. *J. Med. Chem.* **2018**, *61* (17), 7640–7656. https://doi.org/10.1021/acs.jmedchem.8b00610.

(14) Hean, D.; Alde, L. G.; Wolf, M. O. Photosalient and Thermosalient Crystalline Hemithioindigo-Anthracene Based Isomeric Photoswitches. *J. Mater. Chem. C* **2021**, *9* (21), 6789–6795. https://doi.org/10.1039/D1TC01358K.

(15) Tong, F.; Xu, W.; Al-Haidar, M.; Kitagawa, D.; Al-Kaysi, R. O.; Bardeen, C. J. Photomechanically Induced Magnetic Field Response by Controlling Molecular Orientation in 9-Methylanthracene Microcrystals. *Angew. Chemie - Int. Ed.* **2018**, *57* (24), 7080–7084. https://doi.org/10.1002/anie.201802423.

(16) Tong, F.; Al-Haidar, M.; Zhu, L.; Al-Kaysi, R. O.; Bardeen, C. J. Photoinduced Peeling of Molecular Crystals. *Chem. Commun.* **2019**, *55* (26), 3709–3712. https://doi.org/10.1039/c8cc10051a.

(17) Al-Kaysi, R. O.; Zhu, L.; Al-Haidar, M.; Al-Muhannah, M. K.; El-Boubbou, K.; Hamdan, T. M.; Bardeen, C. J. Chemical Reaction Method for Growing Photomechanical Organic Microcrystals. In *CrystEngComm*; Royal Society of Chemistry, 2015; Vol. 17, pp 8835–8842. https://doi.org/10.1039/c4ce02387k.

(18) Tong, F.; Qu, D. H. Engineering Shapes and Sizes of Molecular Crystals to Achieve Versatile Photomechanical Behaviors. *Langmuir*. April 11, 2022, pp 4793–4801. https://doi.org/10.1021/acs.langmuir.2c00414.